Molecular gas and star formation in early-type galaxies

Alison F. Crocker[1,2], Martin Bureau[2], Lisa M. Young[3,4], Francoise Combes[5]

[1] *Department of Astrophysics, University of Massachusetts, 710 North Pleasant Street, Amherst, MA, 01003*
[2] *Sub-Department of Astrophysics, University of Oxford, Denys Wilkinson Building, Keble Road, Oxford OX1 3RH*
[3] *Physics Department, New Mexico Institute of Mining and Technology, Socorro, NM 87801, U.S.A.*
[4] *Adjunct Astronomer at the National Radio Astronomy Observatory ???????*
[5] *Observatoire de Paris, LERMA, 61 Av. de l'Observatoire, 75014, Paris, France*

ABSTRACT

We present new mm interferometric and optical integral-field unit (IFU) observations and construct a sample of 12 elliptical (E) and lenticular (S0) galaxies with molecular gas which have both CO and optical maps. The galaxies contain 2×10^7 to 5×10^9 M$_\odot$ of molecular gas distributed primarily in central discs or rings (radii 0.5 to 4 kpc). The molecular gas distributions are always coincident with distributions of optically-obscuring dust that reveal tightly-wound spiral structures in many cases. The ionised gas always approximately corotates with the molecular gas, evidencing a link between these two gas components, yet star formation is not always the dominant ionisation source. The galaxies with less molecular gas tend to have [O III]/Hβ emission-line ratios at high values not expected for star formation. Most E/S0s with molecular gas have young or intermediate age stellar populations based on optical colours, ultraviolet colours and absorption linestrengths. The few that appear purely old lie close to the limit where such populations would be undetectable based on the mass fractions of expected young to observed old stars. The 8μm polycyclic aromatic hydrocarbon (PAH) and 24μm emission yield similar star formation rate estimates of E/S0s, but the total infrared overpredicts the rate due to a contribution to dust heating from older stars. The radio-far infrared relation also has much more scatter than for other star-forming galaxies. However, despite these biases and additional scatter, the derived star formation rates locate the E/S0 galaxies within the large range of the Schmidt-Kennicutt and constant efficiency star formation laws. Thus the star formation process in E/S0s is not overwhelmingly different than in other star-forming galaxies, although one of the more reliable tracers (24μm) points to a possible lower star-formation efficiency at a given gas surface density.

Key words: galaxies: elliptical and lenticular, cD – galaxies: ISM – galaxies: stellar content – galaxies: evolution – galaxies: kinematics and dynamics

1 INTRODUCTION

Traditionally, much attention has been given to the homogeneity of elliptical and lenticular (hereafter early-type or E/S0) galaxies. Most famously, these galaxies lie on a surface within the volume space of effective radius, mean surface brightness and central velocity dispersion (the Fundamental Plane; e. g. Faber et al. 1987; Dressler et al. 1987; Djorgovski & Davis 1987). Early-type galaxies also follow a tight colour-magnitude relation, brighter galaxies being redder (e. g. Baum 1959; Visvanathan & Sandage 1977). The small scatter in this relation requires the stellar content of the galaxies to be fairly uniform and predominantly old (e. g. Bower, Lucey & Ellis 1992). The interpretation of absorption linestrength indices shows that age, metallicity and alpha-

element enhancement all depend smoothly on galaxy mass, more massive galaxies being older, more metal-rich and more alpha-element enhanced (Thomas et al. 2005). Initial observations showed that early-type galaxies as a group lack a significant cool or cold interstellar medium (ISM), with both atomic hydrogen (HI) and carbon-monoxide (CO) non-detections (Faber & Gallagher 1976; Johnson & Gottesman 1979).

However, observations over the past few decades have also gradually revealed the individuality of early-type galaxies. In terms of radial structure, some E/S0s have cuspy cores or missing light at small radii, while others appear coreless (e. g. Kormendy et al. 2009). Some have very little ordered rotation while others rotate quickly (quantifiable with the specific angular-momentum proxy λ_R; Emsellem et al. 2007).

Stellar populations and all measurements of the gas phase also show a wide spread. Despite their generally uniform optical colours, a range in stellar population ages (particularly towards young ages) is found for E/S0 galaxies through the analysis of absorption linestrengths (e. g. Trager et al. 2000) and ultraviolet-optical colours (e. g. Yi et al. 2005). Ionised gas exhibits a remarkable complexity in early-type galaxies, with different distributions, luminosities, line ratios and equivalent widths not obviously correlated to any particular galaxy property (Sarzi et al. 2006, 2010). Molecular gas, H I and warm dust have all now been detected in a significant fraction of early-type galaxies, with no strong dependence on galaxy luminosity or environment, except for the lack of atomic hydrogen in clusters (e. g. Knapp at al. 1989; Morganti et al. 2006; Combes et al. 2007, Oosterloo et al. in preparation, Young et al. in preparation).

Of course, several of these varying properties are likely to be related. In particular, galaxies with molecular gas reservoirs are expected to be star-forming. This star formation should naturally lead to ionised gas and young stellar populations. However, little is currently known about the origin and evolution of the cold gas and the young stars in E/S0s. Single-dish studies of the molecular gas show that the gas mass does not correlate as well with the blue luminosity of early-types as it does for spirals (Knapp & Rupen 1996; Combes et al. 2007). However, the molecular gas mass is tightly correlated with the far-infrared (FIR) luminosity, matching the correlation for spiral galaxies (Wiklind & Henkel 1989, 1995; Combes et al. 2007). This match suggests that the star formation efficiency is the same in early-type galaxies as it is in spirals, implying that a given amount of molecular gas transforms into the same amount of stars per unit time. However, caution is necessary as theory predicts that the general interstellar radiation field (ISRF) of early-type galaxies should be of sufficient strength to heat the dust observed without requiring any young stars (Jura 1982). In this case, the close relation between molecular gas mass and FIR luminosity simply arises through a constant molecular gas to dust ratio.

Despite these single-dish based efforts, many questions regarding cold gas and star formation in early-type galaxies remain. First, where does the gas come from? Predictions of internal stellar mass loss would provide more gas than is observed if this gas were capable of cooling (e. g. Faber & Gallagher 1976). Most galaxies have far too little gas to match these naive predictions, but several galaxies with interferometric CO maps (revealing the direction of rotation) show that the gas origin is at least consistent with such internal stellar mass loss (Young 2002; Young, Bureau & Cappellari 2008). Of course, some clear cases in which the misalignment of the molecular gas rotation with respect to the stellar rotation indicates external accretion are also documented (Young et al. 2008; Crocker et al. 2008). A large statistical sample with interferometric CO data is thus needed to infer the relative importance of internal versus external accretion processes.

A second major question is: how does star formation proceed in E/S0 galaxies? As mentioned above, the good FIR-CO correlation need not arise from star formation if other dust-heating sources are present. Moreover, some early-type galaxies do not seem to be forming stars as efficiently as predicted. Okuda et al. (2005) argue that the

molecular gas observed in the centre of NGC 383 is stable to gravitational collapse and thus not forming stars. Infrared (Young, Bendo & Lucero 2009) and radio (Lucero & Young 2007) observations of NGC 2320 also do not obviously indicate star formation from its massive molecular disc. Theoretical models from Kawata et al. (2007) suggest that circumnuclear discs in massive galaxies are more stable than those in less massive galaxies. Moreover, a recent cosmological simulation shows that the potential of a massive spheroid can significantly reduce the star formation efficiency of a gas disc ('morphological quenching'; Martig et al. 2009). Further investigations into the connection between molecular gas and star formation in early-type galaxies are thus needed.

If star formation from molecular gas were the dominant property of early-type galaxies, they probably would not be classified as early-type. As such, the molecular gas and star formation are always subtle features and require deeper and more specific observations to investigate in detail. An important step in this direction is to obtain resolved maps of the cold gas, the star formation and the stellar populations. The goal of this study is thus to use interferometric CO maps and optical integral-field unit (IFU) maps to compare the molecular gas to the ionised gas, stellar populations and stellar kinematics in a sample of early-type galaxies. In doing so, we thoroughly investigate the connection between the molecular gas and star formation. Our moderate sample size allows us to focus on individual galaxies when warranted, as well as to try to create a global picture of the evolution of early-types with molecular gas.

This paper presents some new mm interferometric data on five galaxies, and investigates the general molecular gas, ionised gas and stellar properties within the sample of twelve early-type galaxies that have both CO maps and IFU data (including literature data). Section 2 describes the sample and Section 3 explains both the interferometric and IFU observations and data reduction. We present the new CO maps of three early-type galaxies in Section 4, as well as characterising two CO non-detections and two mm continuum detections. In Section 5, we switch from the analysis of individual galaxies to a consideration of the sample as a whole, investigating the properties of the molecular gas alone and with respect to the IFU data. Section 6 presents an analysis of the origin of the cold gas and then delves into the star formation properties of these galaxies, investigating the validity of various star formation tracers and comparing our sample galaxies to the predictions of the Schmidt-Kennicutt and constant efficiency star formation laws. We summarise our findings in Section 7.

2   SAMPLE

Our goal is to obtain as large a sample as possible of early-type galaxies with both interferometric CO data and optical IFU maps. We start from the IFU observations of the the the SAURON instrument, which consist of the main SAURON sample of 48 E and S0 galaxies and a handful of other E and S0 galaxies observed as 'specials' for particular projects (most of these are listed in Table 3 of Cappellari et al. 2007). The selection of the main sample was designed to be representative (as opposed to complete), with equal numbers of Es
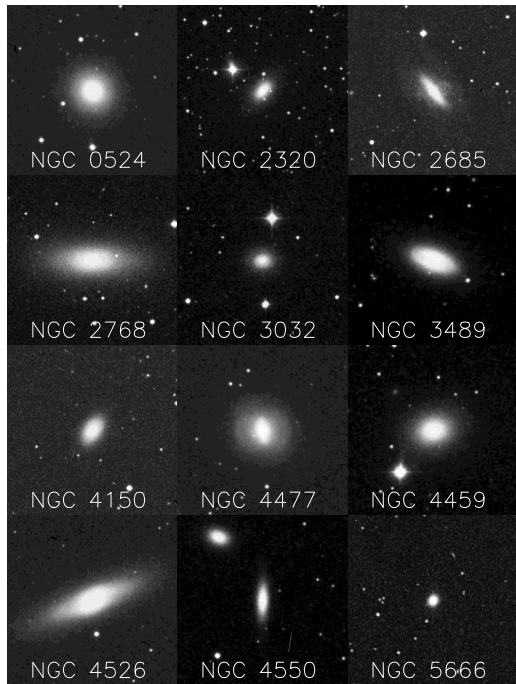
Figure 1. DSS *R*-band images of the **12** sample E/S0 galaxies with molecular gas. Each image is $7' \times 7'$.

and S0s and cluster and non-cluster members, additionally trying to uniformly populate ellipticity-magnitude space (de Zeeuw et al. 2002).

Combining a detection campaign with the Institut de Radioastronomie Millimétrique (IRAM) 30m telescope (Combes et al. 2007) and data from the literature, 13/48 galaxies of the main sample are detected in CO from single-dish measurements. Follow-ups to obtain interferometric molecular gas data have mapped 4 galaxies with the Berkeley-Illinois-Maryland Array (BIMA; Young et al. 2008) and 7 galaxies with the IRAM Plateau de Bure Interferometer (PdBI; Crocker et al. 2008, 2009, 5 presented in this paper). Two galaxies observed with PdBI turn out to be non-detections (described below). One galaxy, NGC 2685, already has interferometric data in the literature (Schinnerer & Scoville 2002). Thus out of the original 13 CO detections from the main SAURON early-type sample, 10 now have interferometric maps, 2 are false single-dish detections and for only one, NGC 3156, we have been unable to obtain interferometric data.

No systematic survey of molecular gas in the SAURON 'specials' sample has been undertaken, but a literature search reveals CO detections for three: NGC 2320, NGC 5666 and NGC 5866 (Wiklind & Henkel 1995; Welch & Sage 2003). NGC 2320 and NGC 5666 both have interferometric CO maps (Young 2002, 2005), so we also include these two galaxies in our sample. As they have not gone through the same selection process, we briefly describe both of them here.

NGC 2320 lies at 83 Mpc, more distant than the SAURON sample limit of 40 Mpc. It is classified as an elliptical in both the RC3 (de Vaucouleurs et al. 1991) and UGC (Nilson 1973) catalogues and is a member of the Abell 569 cluster.

Table 1. Observing parameters

Galaxy (NGC)	Date	Config.	Ant.	Receiver	T_{sys} (K)
524	24/08/07	D	5	new: 3mm	250
	21/12/07	C	6	new: 3mm	200
3489	23/04/07	C	6	new: 3mm	225
	23/10/08	D	6	new: 3mm	250
	24/10/08	D	6	new: 3mm	350
4278	24/12/05	C	6	old	400, 300
	01/11/07	D	6	new: 1mm	200
4477	09/01/06	C	5/6	old	250, 300
	30/04/06	D	6	old	225, 350
7457	29/06/07	D	4/5	new: 3mm	200
	13/07/07	D	5	new: 3mm	250

NGC 5666 (at 35 Mpc) is a difficult galaxy to classify. Donzelli & Davoust (2003) conclude that NGC 5666 has too much gas and spiral structure to be a true early-type, but also has too high a bulge-to-total ratio and too old stellar populations for a normal Scd galaxy. An $r^{1/4}$ law fits the Spitzer Multiband Imaging Photometer (MIPS) 24 μm surface brightness profile reasonably well (based on data from Young et al. 2009), hinting at the dominance of a classic de Vaucouleurs profile. We thus include NGC 5666 in our sample, but remain aware of its uncertain morphology. In particular, we note that it did not meet the visual early-type selection criteria for the complete Atlas3D sample, which follows upon the SAURON survey (Cappellari et al. in preparation).

We therefore have a total of 12 galaxies with both IFU and CO maps (10 from the main sample and 2 'specials'). Unfortunately the CO distribution of NGC 2685 lies in a polar ring outside of the region mapped with the SAURON IFU, so sometimes we will not be able to discuss this galaxy with the rest of the sample. Additionally, the CO-detected but unmapped galaxy from the main SAURON sample, NGC 3156, is included when information on the CO distribution is not required. The inclusion of the two 'special' galaxies complicates the sample, but we are primarily interested in considering the range of molecular gas and star formation properties in E/S0s and so want the largest sample size possible. When the statistics of the properties are important, we will limit the sample to the galaxies from the main SAURON sample. However, more detailed work in this vein requires a much larger (and complete) sample. Digital Sky Survey (DSS) *R*-band images for the 12 sample galaxies are shown in Fig. 1.

3   OBSERVATIONS AND DATA REDUCTION

3.1   CO observations and data analysis

We observed five galaxies (NGC 524, NGC 3489, NGC 4278, NGC 4477 and NGC 7457) in the C and D configurations at the PdBI. Observing parameters for individual galaxies are listed in Table 1. The receivers were upgraded in December 2006. After this point, the CO(2-1) and CO(1-0) lines could no longer be simultaneously observed. The correlator configuration before December 2006 had a total bandwidth of 580 MHz and 1.25 MHz resolution. Since December 2006, the total bandwidth is 950 MHz with 2.5 MHz resolution. During the observations, the correlator was regularly calibrated by a noise source inserted in the IF system.

Table 2. Mapping parameters

Galaxy (NGC)	CO Line	Clean Beam	Pixel Size	V_{sys} (km s^{-1})
524	(1-0)	$2''8 \times 2''6$	$0''68 \times 0''68$	2379
3489	(1-0)	$3''1 \times 2''9$	$0''75 \times 0''75$	713
4278	(2-1)	$1''7 \times 1''5$	$0''40 \times 0''40$	649
4477	(1-0)	$3''3 \times 2''6$	$0''75 \times 0''75$	1355
	(2-1)	$1''6 \times 1''2$	$0''375 \times 0''375$	1355
7457	(1-0)	$4''2 \times 3''5$	$1''00 \times 1''00$	812

Note: Systemic velocities from NASA/IPAC Extragalactic Database (NED), except for NGC 3489 where it is taken from the SAURON stellar kinematics (Emsellem et al. 2004).

The data were reduced with the Grenoble Image and Line Data Analysis System (GILDAS) software packages CLIC and MAPPING (Guilloteau & Lucas 2000). Using CLIC, we first calibrated the data using the standard pipeline for bandpass calibration, phase calibration, absolute flux calibration and amplitude calibration. Data obtained during periods of bad weather were flagged and then ignored. After calibration, we used MAPPING to create data cubes with velocity planes separated by 20 km s^{-1} and natural weighting. The pixel size for each map is based upon the size of the beam, both of which are reported in Table 2. For the three galaxies with detected CO emission, NGC 524, NGC 3489 and NGC 4477, we cleaned using the Högbom method (Högbom 1974). We stopped cleaning in each velocity plane after the brightest residual pixel had a value lower than the rms noise of the uncleaned datacube. We used the MIRIAD task `contsub` to subtract the continuum present in NGC 524.

For the galaxies with detected CO emission, we made integrated intensity and mean velocity maps using the smoothed-mask method (see Fig. 2). First a smoothed cube is created by Hanning smoothing in velocity and smoothing with a 4-pixel circular Gaussian spatially. Then, all values in this cube below three times the rms noise are masked. This mask is then used on the original cube to compute the moments. With the extent of the molecular gas defined by the 0th moment map, we then integrate over this region for all velocities to obtain a total spectrum for each galaxy. These spectra are shown in Fig. 3, where the shaded regions indicate the velocity widths integrated over to obtain the total fluxes.

We compute the molecular hydrogen masses from the total CO(1-0) fluxes using the formula $M(H_2) = (1.22 \times 10^4\ M_\odot) D^2 \cdot S_{CO}$, where D is the distance measured in Mpc and S_{CO} is the total CO(1-0) flux in Jy km s^{-1}. This formula comes from using the standard CO to H$_2$ conversion ratio $N(H_2)/I(CO) = 3 \times 10^{20}$ cm^{-2} (K km s^{-1})$^{-1}$, where $N(H_2)$ is the column density of H$_2$ and $I(CO)$ is the CO(1-0) intensity in K km s^{-1} based on the main-beam temperature, T_{mb}.

For the non-detected galaxies, we integrated the datacube over a central 5$''$ radius aperture, obtaining the spectra shown in Fig. 3. We then measured the noise in each spectrum and obtained a flux upper limit by the formula $3\,\sigma_{rms}\sqrt{n}$, where n is the number of channels in which emission is expected. The velocity width used for NGC 4278 is -240 to 240 km s^{-1} (25 channels) and for NGC 7457 it is -140 to 140 km s^{-1} (15 channels) about the systemic velocity. These are based on the maximum velocity seen in

the ionised gas within the SAURON field-of-view. We convert these CO flux upper limits to molecular gas masses using the same formula as for the detected galaxies. These mass upper limits are listed in Table 3.

To constrain the continuum emission, we created continuum uv tables for each galaxy using all frequencies without any detected line emission. For the galaxies with line emission, we selected channels at least 40 km s^{-1} away from the highest and lowest velocity channels with any line emission. The very edges of the bandwidth were also avoided. No continuum emission was detected in NGC 3489, NGC 4477 or NGC 7457. In NGC 524 and NGC 4278, we fit the continuum with a point source model in the uv plane. The fit results give the flux and location of the point source. In both cases, a point source located at the galaxy centre was a good fit. For NGC 4278, we have observations at 1 mm separated by a period of nearly two years. We created separate uv tables for the two observations and find that the fluxes are different by a factor of about 2, even after special care is given to the flux calibrations.

3.2 SAURON IFU observations and data analysis

The SAURON IFU data have been presented in a series of papers: the stellar kinematics in Emsellem et al. (2004), the ionised gas in Sarzi et al. (2006, 2010), the absorption linestrengths in Kuntschner et al. (2006) and the stellar populations in Kuntschner et al. (2010). However, since these papers have been published (except Kuntschner et al. 2010), a new stellar template library consisting of single stellar population (SSP) models from Vazdekis et al. (in preparation, based on MILES stellar spectra from Sánchez-Blázquez et al. 2006) and emission-free SAURON spectra has been used for the data analysis (see Sarzi et al. 2010; Kuntschner et al. 2010). The data we discuss and the maps we present here are all based upon the new stellar template library.

NGC 2320 and NGC 5666 (outside of the main SAURON sample) were also run through the SAURON reduction and analysis pipeline, with only minor modifications to accommodate the higher redshift of NGC 2320 (in particular, the disappearance of the $\lambda 5170$ Å Mg triplet). As their SAURON data have not previously been presented, we present the SAURON maps for these galaxies in Appendix 1, along with some short notes on both galaxies.

4 MILLIMETRE RESULTS

We detect CO emission in NGC 524, NGC 3489 and NGC 4477, but not in NGC 4278 or NGC 7457. Continuum emission is detected in both NGC 524 and NGC 4278. In NGC 4278, we infer an intrinsic variation of the continuum emission associated with its AGN (Section 4.4). Here we present the millimetre data for these five individual galaxies.

4.1 Comparison to single-dish observations

Before discussing the results for each galaxy, we compare the interferometric spectra and fluxes to those obtained from the IRAM 30m single-dish data. The single-dish data of NGC 3489, NGC 4477 and NGC 4278 were published in
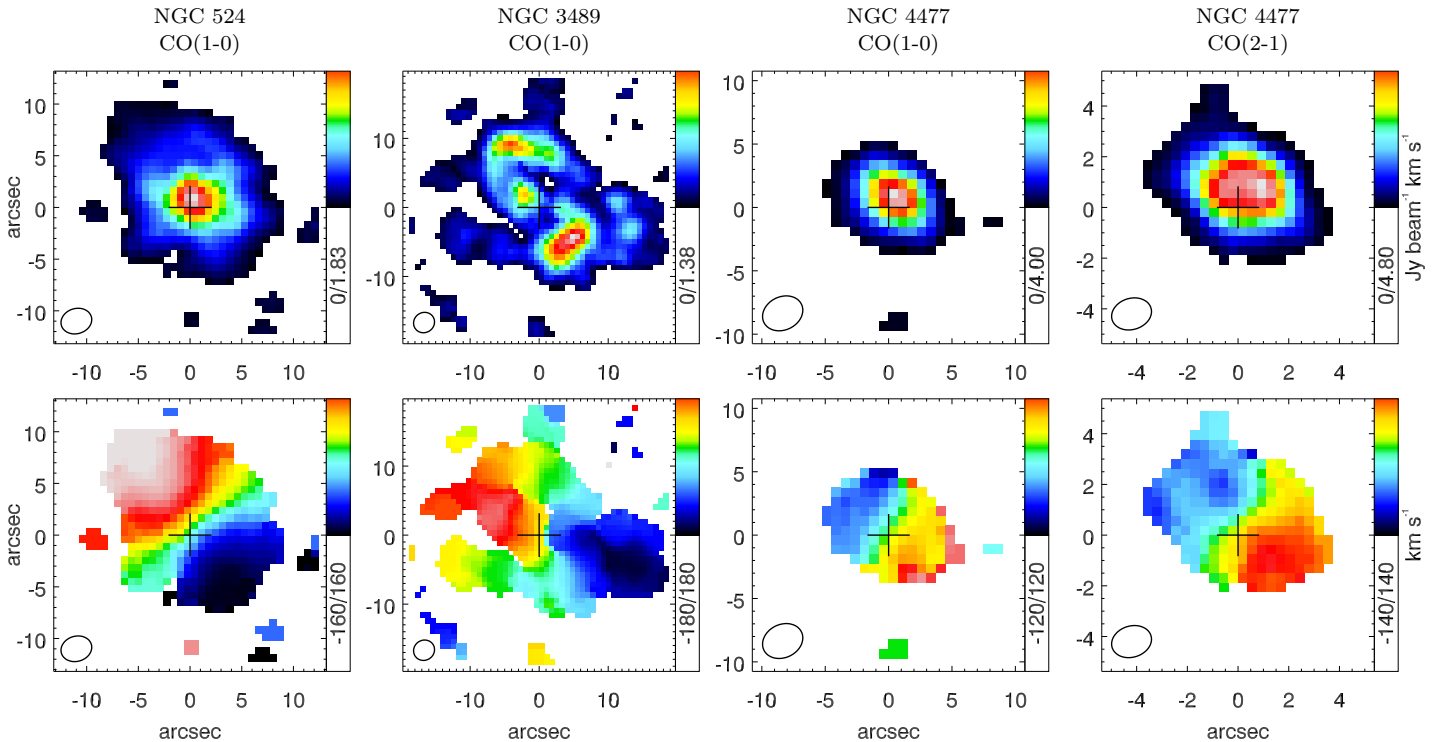
Figure 2. *Top:* Integrated intensity maps (Jy beam^{-1} km s^{-1}). *Bottom:* Mean velocity maps (km s^{-1}), relative to the systemic velocity of each galaxy (see values listed in Table 2). White pixels have been masked according to the method described in Section 3.1. The beam size is indicated in the lower left-hand corner of each panel and the cross marks the centre of the galaxy from the Two Micron All Sky Survey (2MASS). Note that the CO(2-1) map for NGC 4477 is on a smaller spatial scale than the CO(1-0) map.

Combes et al. (2007) while those of NGC 524 and NGC 7457 have been obtained more recently, to be published in Young et al. (in preparation). The single-dish spectra are plotted as dashed lines over the interferometric spectra in Fig. 3.

In light of the noise in both the single-dish and interferometric spectra and the 10-20% calibration uncertainty in each, the agreement between the spectra is good. However, we note large ($\approx$50%) disagreements between the molecular masses derived for the two galaxies NGC 524 and NGC 3489. For NGC 524, the interferometer recovers less flux than the single dish. The interferometer may have resolved out some flux, possible for the relatively extended gas distribution in this galaxy. Additionally, the velocity window we integrate over is narrower than that of Young et al. (in preparation), who include some channels at higher velocities with positive intensities. For NGC 3489, conversely, the interferometer recovers more flux than the single-dish observations. This flux discrepancy is due to the single-dish detection only being fit to the peak seen at negative velocities, while we see definite emission up to 140 km s^{-1}. Noise is the most likely culprit, making the emission at negative velocities more prominent in the single-dish spectrum. A mild pointing error is also possible, especially given the extended CO distribution revealed in the interferometric map.

Our interferometric spectra show no sign of CO(1-0) emission in either NGC 4278 or NGC 7457. The observations of NGC 4278 give an upper limit of 6.9×10^6 M$_\odot$ of molecular gas, three times less than the 2.3×10^7 M$_\odot$ reported from the single-dish observations. For this galaxy, the single-dish detection is suspect because neither of the

two CO lines 'detected' is at the galaxy's systemic velocity; the CO(1-0) is reported to be centred at 185 km s^{-1} and the CO(2-1) at -112 km s^{-1}. We are thus confident in our non-detection. NGC 7457 was reported to contain 3.8×10^7 M$_\odot$ of molecular gas within the 15″ beam of the Nobeyama 45m telescope by Taniguchi et al. (1994). Welch & Sage (2003) reported 4.7×10^6 M$_\odot$ within the 55″ beam of the NRAO 12m telescope (both values corrected for our X$_{CO}$ factor and distance). However, both of these detections have extremely low signal-to-noise ratios and our observations at the PdBI give an upper limit of 1.8×10^6 M$_\odot$. We also note that this non-detection is corroborated by the new spectrum from the IRAM 30m of Young et al. (in preparation), shown as a dashed line in Fig. 3.

4.2 Individual galaxies

4.2.1 NGC 524

NGC 524 hosts a 1.1 kpc radius molecular gas disc of 6.7×10^7 M$_\odot$ according to the PdBI map (see Fig. 2). The molecular disc coincides with a tightly wound spiral of dust seen in a F555W unsharp-masked image from the Hubble Space Telescope Wide-Field Planetary Camera 2 (HST/WFPC2; see Fig. 4). The CO velocity map shows an ordered velocity field with a surprisingly large maximum velocity for such a face-on configuration. While Sil'chenko (2000) interprets the similarly large velocities she finds for the ionised gas as indicating a kinematically decoupled gas component, the CO and ionised gas velocities actually agree
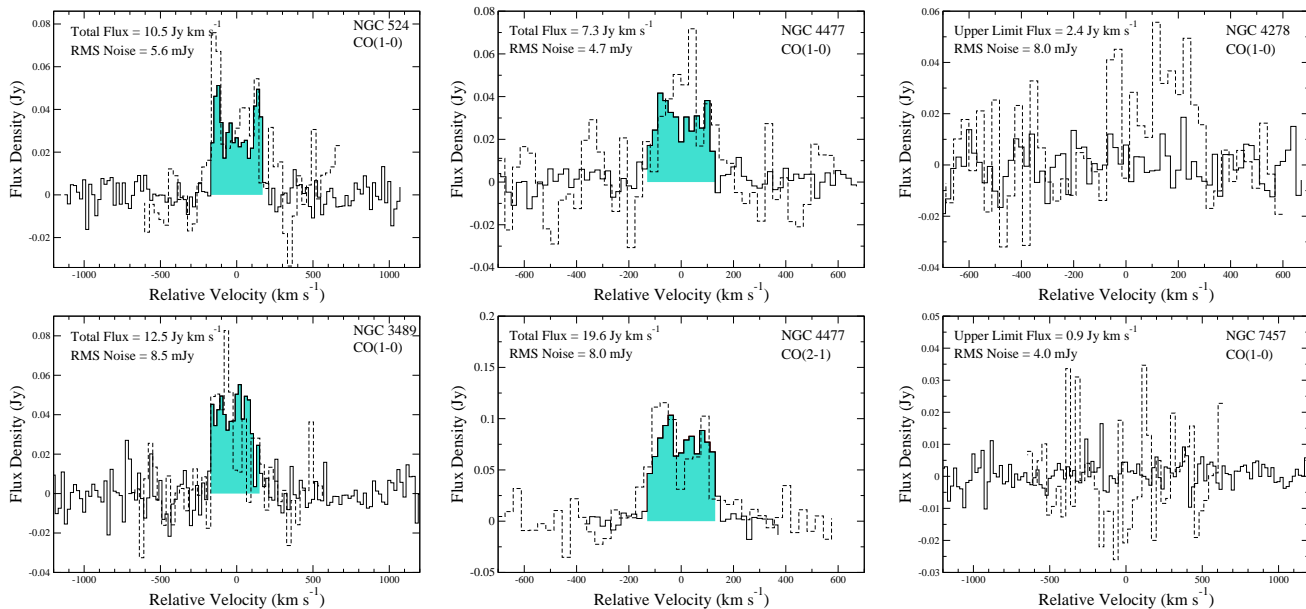
Figure 3. PdBI spectra integrated over the regions with detected emission (detections) or a central 5″ radius aperture (non-detections). For the detected galaxies, the shaded area represents the velocity range integrated over to obtain the total flux. The dashed lines show the single-dish data from the IRAM 30m telescope of Combes et al. (2007) and Young et al. (in preparation).

well with the circular velocities (maximum 465 km s^{-1}) computed by assuming the multi-Gaussian expansion (MGE) mass distribution, dynamical mass-to-light ratio and inclination derived in Cappellari et al. (2006) from a model of NGC 524's stellar kinematics. At 6″, this model predicts a velocity of 150 km s^{-1}, which is very close to the 160 km s^{-1} we observe. Thus, the gas is not kinematically decoupled, NGC 524 is simply a massive galaxy.

NGC 524 has central 3mm continuum emission, with a flux density of $4.5 \pm 0.2 \pm 0.9$ mJy (random and systematic error). It has previously been detected in radio continuum at 1.4, 5 and 8.4 GHz (Condon et al. 1998; Filho, Barthel & Ho 2002; Filho et al. 2004). The 5 GHz Very Long Baseline Array (VLBA) observations show that NGC 524's radio core is compact on milliarcsecond-scales, clearly indicating an active galactic nucleus (AGN). With a beam of 2″.66 × 2″.47, the 8.4 GHz VLA observations are very well matched to the resolution of our 3mm observations. At this resolution, the flux density increases from 1.95 mJy at 8.4 GHz to 4.5 mJy at 3 mm (115 GHz). A maximum of 1.5 mJy at 3mm can be explained by dust based on the Infrared Astronomical Satellite (IRAS) 100 and 60 μm data points, so most of the emission at 3 mm must originate from self-absorbed synchrotron emission from the AGN (e. g. Krips et al. 2007).

4.2.2   NGC 3489

Unlike any other early-type galaxy, NGC 3489's 2.1×10^7 M$_\odot$ of molecular gas is clearly resolved into an extended spiral-like pattern (Fig. 2). The spiral consists of an arc to the north-east (≈ 570 pc from the centre), a nearly central clump (≈ 170 pc to the north-east) and an arc to the south-west (≈ 460 pc). The three blobs (one very faint) to the west are likely an extension of the northern spiral arm. The galaxy centre is determined from the Two Micron All Sky Survey

(2MASS), so it should be accurate to 2″, implying that the nearly-central clump is indeed offset and cannot be directly associated with the galaxy nucleus. This clumpy and not settled distribution suggest that the gas has been recently acquired or recently disturbed. The molecular gas velocity map shows general corotation with both the ionised gas and the stars. However, to the south, negative relative velocities extend further east than might be expected, similar to a feature seen in the ionised gas map. This velocity irregularity also suggests the recent acquisition or disruption of the gas.

4.2.3   NGC 4477

The barred S0 galaxy NGC 4477 shows a small nuclear ring of 2.3×10^7 M$_\odot$ of molecular gas. This H$_2$ mass matches the IRAM 30m value within the errors. While the large CO(1-0) beam makes the gas appear centrally peaked, the CO(2-1) integrated intensity map shows a hint of ring structure (Fig. 2), which is then much more visible in the integrated clean component map (no convolution by the 'clean beam'; Fig. 5). The size and location of this molecular gas ring agrees well with the ring-like structure seen in the optically obscuring dust (Fig. 4).

4.2.4   NGC 4278

The CO observations of NGC 4278 give an upper limit of 6.9×10^6 M$_\odot$ of molecular gas.

The 1 mm continuum observations reveal a central unresolved point source in both the December 2005 and November 2007 runs. However, the flux of this source is 34 mJy in December 2005 and 65 mJy in November 2007. Sometime between November 2002 and May 2003, Doi et al. (2005) detected 3 mm (96 GHz) continuum at 57 mJy using the Nobeyama Millimetre Array. As all these observa-
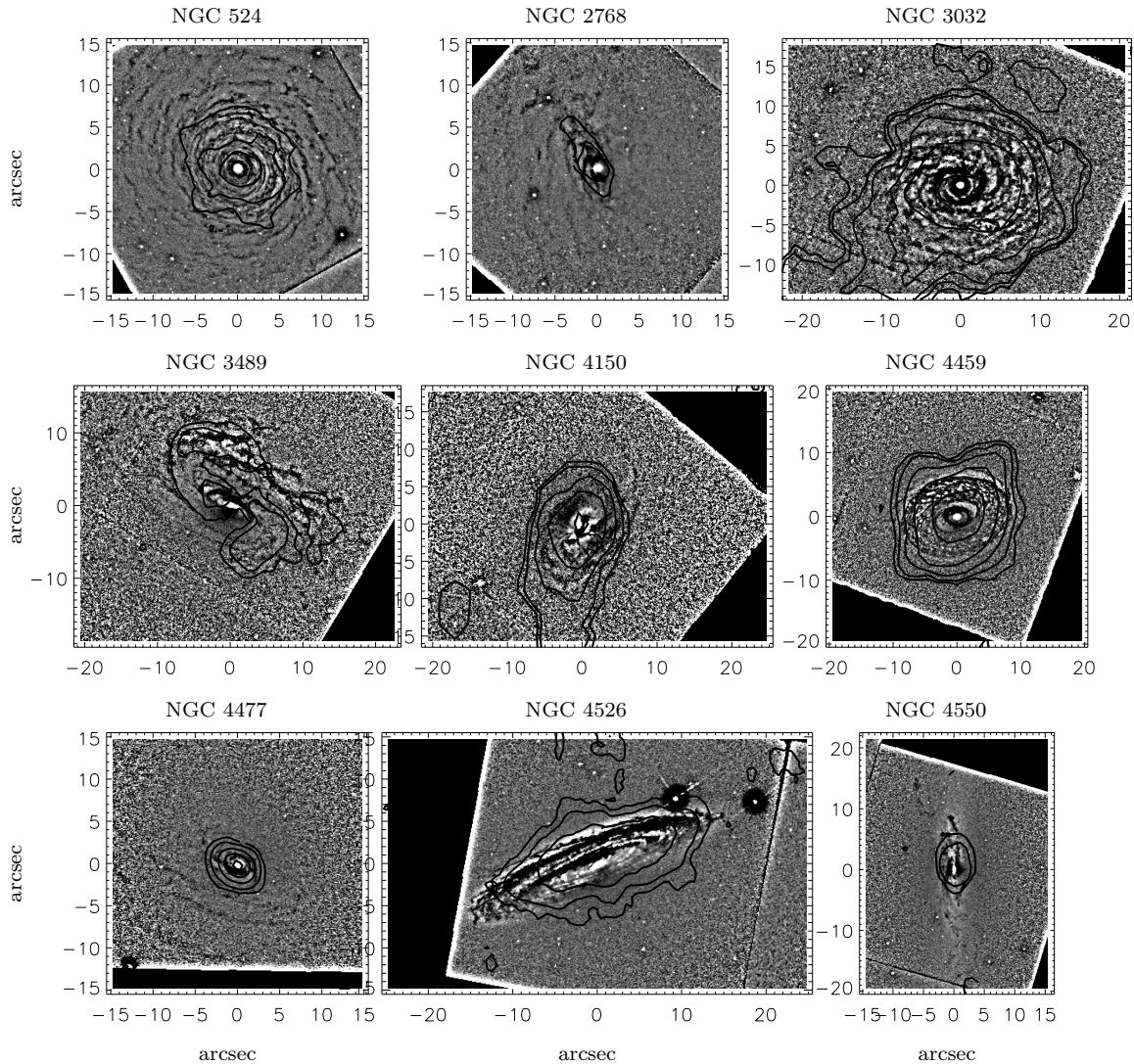
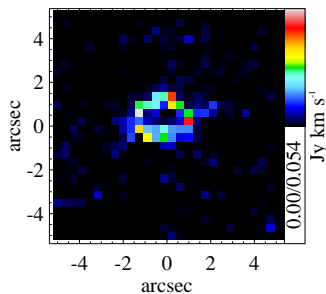**Figure 4.** Unsharp-masked HST WFPC2 F555W images showing optically obscuring dust. CO(1-0) contours are overlaid in black.

Figure 5. Centre of NGC 4477. Integrated clean component map of NGC 4477 in CO(2-1). The ring structure is clear, with a radius of $1.''3$ (≈ 100 pc).

tions should have a flux accurate to around 20%, we think such variation in the mm continuum of NGC 4278 is real. NGC 4278 has a known AGN, with a compact X-ray source (Colbert & Mushotzky 1999) and possible sub-parsec-scale radio jets (Giovannini et al. 2001). Periods of variability of

the radio emission have been reported previously, for example Schilizzi et al. (1983) report a 25% increase in 6 cm radio emission between February 1980 and April 1981.

4.2.5 NGC 7457

The PdBI observations limit the amount of molecular gas in NGC 7457 to 1.8×10^6 M$_\odot$. The absence of significant molecular gas also fits well with the low level of ionised emission and the lack of optically obscuring dust in this galaxy (Sarzi et al. 2006).

5 ANALYSIS

5.1 Distribution of molecular gas

The set of CO maps presented here and in Schinnerer & Scoville (2002), Young (2002), Young (2005), Young et al. (2008), Crocker et al. (2008) and Crocker et al. (2009) reveal the distribution of the molecular gas in early-type galaxies.

Table 4. CO-based molecular gas properties.

Galaxy	Instrument	D (Mpc)	M_{H_2} ($M_\odot$)	R_{H_2} (kpc)	Σ_{H_2} ($M_\odot$) pc^{-2}	H_2 Morphology	CO Ref.	Dust Map Ref.
NGC 524	PdBI	23.3	6.7×10^7	1.1	23	face-on disc	(1)	(1)
NGC 2320	BIMA	83	4.6×10^9	4.0	120	edge-on disc	(2)	(2)
NGC 2685	OVRO	15.0	2.3×10^7	2.5	–	extended polar ring	(3)	(3)
NGC 2768	PdBI	21.8	6.3×10^7	0.6	68	polar ring/disc	(4)	(1)
NGC 3032	BIMA	21.4	5.0×10^8	1.5	96	disc	(5)	(1)
NGC 3156	30m	21.8	2.2×10^7	–	–	–	(6)	(3)
NGC 3489	PdBI	11.8	2.1×10^7	0.8	14	spiral	(1)	(1)
NGC 4150	BIMA	13.4	5.5×10^7	0.6	70	ring/disc	(5)	(1)
NGC 4459	BIMA	16.1	1.7×10^8	1.0	72	disc	(5)	(1)
NGC 4477	PdBI	16.5	2.3×10^7	0.4	63	ring	(1)	(1)
NGC 4526	BIMA	16.4	5.7×10^8	1.0	230	disc	(5)	(1)
NGC 4550	PdBI	15.5	7.9×10^6	0.4	24	lopsided ring/disc	(7)	(1)
NGC 5666	BIMA	35	5.6×10^8	2.7	33	ring	(8)	(2)

CO REFERENCES: (1) this paper, (2) Young (2005), (3) Schinnerer & Scoville (2002), (4) Crocker et al. (2008), (5) Young et al. (2008), (6) Combes et al. (2007), (7) Crocker et al. (2009), (8) Young (2002). DUST MAP REFERENCES: (1) Fig. 4, (2) Young et al. (2009), (3) Sarzi et al. (2006). NOTE: The molecular gas mass of NGC 2685 was recalculated using our I_{CO} factor.

Table 3. CO fluxes and molecular gas mass estimates from PdBI.

Galaxy	Flux (Jy km s^{-1})	M_{H_2} ($M_\odot$)	H_2 radius (kpc)
NGC 524	10.5	6.7×10^7	1.1
NGC 3489	12.5	2.1×10^7	0.8
NGC 4278	< 2.4	$< 6.9 \times 10^6$	–
NGC 4477	7.3	2.3×10^7	0.4
NGC 7457	< 0.9	$< 1.8 \times 10^6$	–

The molecular gas is mostly found in central discs or rings (see Table 4), although the map resolutions are usually too poor to distinguish between these structures. The two known exceptions to the central disc/ring rule are the molecular spiral of NGC 3489 and the spots of CO emission in the extended H I polar ring of NGC 2685 (at a radius of $34'' =$ 2.5 kpc). Two other galaxies, NGC 2768 and NGC 4150, also show faint tails of CO emission. Other interferometric CO maps in the literature also suggest that a central disc and/or ring is the most common distribution for the molecular gas of early-type galaxies (Wiklind et al. 1997; Young 2002, 2005; Okuda et al. 2005).

However, there is a bias toward detecting central molecular structures because almost all interferometric targets have been selected based on central single-dish observations. For example, the CO emission in the polar ring of NGC 2685 would not have been detected by a central observation using the IRAM 30m telescope (instead its molecular gas was detected in an interferometric study of its H I ring by Schinnerer & Scoville 2002). H I and UV observations prove that outlying molecular gas does exist in a fraction of early-type galaxies, assuming molecular gas is necessary for star formation. For example, two E/S0 galaxies from the SAURON sample, NGC 2974 and NGC 4262, have substantial H I rings at radii of ≈ 8 and ≈ 13 kpc, respectively (Weijmans et al. 2008, Oosterloo et al. in preparation). Within these rings, clumps of UV emission are seen, which must be due to knots of young stars (<100 Myr) recently formed from molecular gas (Jeong et al. 2007). These outer star-forming rings are

similar to the case of ESO 381-47, thoroughly analysed in Donovan et al. (2009).

Attempting to quantify the statistics of where molecular gas is found in E/S0 galaxies requires an unbiased sample. Taking the SAURON representative sample of 48 early-type galaxies, 10/48 have centrally-detected CO while 3/48 present evidence of outlying molecular gas (NGC 2685, NGC 2974 and NGC 4262). Although a larger and complete sample will solidify these numbers considerably, these fractions provide a rough estimate of where molecular gas is found in early-type galaxies.

The resolution limit of the interferometric observations means that the molecular gas may lie in more detailed structures than the CO maps currently probe. A suggestion of these structures is indicated by the dust maps shown in Fig. 4 (unsharp-masked optical images). In all cases, the gas and dust appear spatially linked. Galaxies with over 10^8 M$_\odot$ of molecular gas have clear flocculent spiral patterns (NGC 3032, NGC 4459 and NGC 4526), while galaxies with less molecular mass have less obscuring dust and the dust structures are less ordered. However, the total molecular mass does not alone determine the appearance of the dust. For example, NGC 524, NGC 2768 and NGC 4150 all have similar molecular gas masses of about 10^8 M$_\odot$, but NGC 524 has an extensive flocculent, tightly-wound spiral dust disc while NGC 2768 has a small polar nuclear ring with extended wisps and NGC 4150 has an irregular, very central dust structure.

None of our sample galaxies have a well-ordered two-arm spiral pattern. Even in the case of NGC 3489, with its molecular two-armed spiral, the dust reveals a multiple-armed more flocculent distribution. However, the absence of such two-arm structure may be a selection effect - galaxies with a strong two-arm spiral in dust and molecular gas are likely to have associated star formation and be classified as Sa or later type galaxies. A combination of the galaxy properties (bar, shape of potential) and the history of the cold gas (time since accretion or cooling) must affect the cold gas and dust morphology. In early-type galaxies, this cold

material is most often found in compact, flocculent spiral or nuclear ring configurations.

We determine an outer radius (R_{H_2}) for the molecular gas based on the radius of largest extent in the CO maps (one-half the largest diameter through the centre; reported in Table 4). We wish to characterise the outer radius for the molecular discs or rings, and so ignore the clear tails of emission seen in some galaxies. However, the R_{H_2} values measured depend critically on the depth and spatial resolution of the CO observations. Ideally, better resolution and sensitivity will allow the measurement of a proper characteristic scale radius for these molecular gas distributions and enable a more consistent study of their extent.

Nevertheless, the mass measured with an interferometer corresponds to the radial limit of the CO observed and we can calculate an average molecular gas density for this region, listed in Table 4. These average molecular gas densities range between 14 and 230 $M_\odot$ pc^{-2}. The lower limit is related to the density at which neutral hydrogen becomes predominantly molecular, which seems to be around 10 $M_\odot$ pc^{-2} (Bigiel et al. 2008). At the high end, densities are approaching the densities of individual molecular clouds.

5.2 Molecular gas and ionised gas

All of our CO-detected sample galaxies are also detected in the Hβ and [O III] optical emission lines. Contours of the molecular gas distributions over the Hβ flux maps from the SAURON IFU (Sarzi et al. 2006) reveal that ionised gas is detected everywhere there is molecular gas (see Fig. 6; except in NGC 524 where the IFU data have lower signal-to-noise ratios due to bad weather). However, in approximately half of the galaxies, the ionised gas extends to larger radii than the molecular gas distribution. For these galaxies, cool gas in the form of atomic hydrogen may extend to these radii and provide the material to be ionised. The detection of H I in nearly all of these galaxies (see Table 7) strengthens this hypothesis. The kinematics of the molecular and ionised gas are always shared (not shown), indicating a strong link between the two gas phases.

Emission-line equivalent width (EW) features are seen in both the [O III] and Hβ lines of many of our sample galaxies. These include central peaks attributable to AGN, ring features associated with star formation, and spiral or filamentary enhancements of unclear origin (Sarzi et al. 2010). However, only the strongly star-forming rings in NGC 3032 and NGC 5666 match the CO distribution. Filaments or spirals of increased EW([O III]) are seen in NGC 2320, NGC 2768, NGC 3489 and NGC 4550, but the molecular gas does not obviously relate to these structures. Furthermore, similar structures are seen in many of the SAURON sample galaxies without molecular gas. Aside from the two strongly star-forming galaxies NGC 3032 and NGC 5666, the EW features are not directly tied to the molecular gas, suggesting it is the source(s) of the ionisation and not the underlying gas density that mediates these structures.

The sources of ionisation of all the SAURON galaxies are discussed at length in Sarzi et al. (2010). The basic conclusions of this work are that 1) AGN cannot dominate the ionisation outside of the central few hundred parsecs (central few arcsec), 2) the shock speeds required for significant shock ionisation are too high given the galaxies' potentials, 3) in-

teraction with the hot gas phase gives a distinct morphology and low-excitation to the ionisation, but is only relevant for the most massive galaxies, 4) low [O III]/Hβ ratios point to ongoing star formation in a few galaxies, 5) young pAGB stars are likely dominant in a few galaxies with a significant young stellar component, and 6) generally, old pAGB stars seem the most likely source of much of the non-star forming ionisation in early-type galaxies. We tabulate the suggested dominant ionisation source of our sample galaxies in Table 5, classifying the two additional special galaxies according to the same principles.

Surprisingly few galaxies of our sample contain gas definitely ionised by star formation (5/13), while the gas in a similar number is ionised by young post-AGB stars (6/13) and the gas in the remaining few is ionised by an AGN or old pAGB stars (2/13; see Table 5). The division between star formation and other types of ionisation is made based on the [O III]/Hβ ratio, since this ratio is generally the only ratio available and is lower for star formation (unless the star-forming gas is of low metallicity, when the ratio remains high). We note that in several of the galaxies ionised by young pAGB stars, the ionised gas is more extended than the CO distribution, further suggesting a source other than star formation is responsible for their ionisation. Total integrated $\log$([O III]/Hβ) ratios of our sample galaxies range from -0.63 to 0.57 (listed in Table 5), while for SAURON galaxies without molecular gas this range is 0.03 to 0.47. For our sample galaxies, the total [O III]/Hβ ratio anti-correlates with the total molecular gas mass (except for NGC 2320; see Fig. 7). Galaxies with less molecular mass have higher [O III]/Hβ ratios similar to those found in galaxies without any detected molecular gas, indicating that star formation does not dominate over other ionisation sources at these lower gas contents.

We note that a possible alternative cause for this trend would be both a higher [O III]/Hβ and a higher X_{CO} factor (thus H$_2$ content currently underpredicted) at low gas-phase metallicities. Early-type galaxies might contain such low-metallicity gas if they have accreted it from a low-mass satellite or other unenriched source. Directly determining the gas phase metallicities would be ideal to investigate this scenario, but this is not possible with the current data. However, the work of Schawinski et al. (2007a) suggests that low-metallicity star-forming gas is rare in E/S0s, as does the relation between IR and Hα star-formation indicators discussed in Section 7.2.4 for our sample. Thus, the anti-correlation observed is more likely explained by star formation dominating the ionisation only when high star formation rates (associated with large molecular gas reservoirs) are reached.

NGC 2320 has the most molecular gas of our sample, but also displays a uniformly high [O III]/Hβ ratio. The balance between ionisation from star formation and other ionisation sources must be different in this galaxy. Either star formation is weaker than expected given its molecular gas content (supported by the lack of extended radio continuum and 24μm emission; Young et al. 2009) or other ionisation processes are particularly strong, possibly its AGN. Further data are needed to distinguish these scenarios, particularly to investigate whether such a larger reservoir of molecular gas could have a very low star formation efficiency.

In summary, we see ionised gas wherever molecular gas is detected and the two gas phases are kinematically aligned
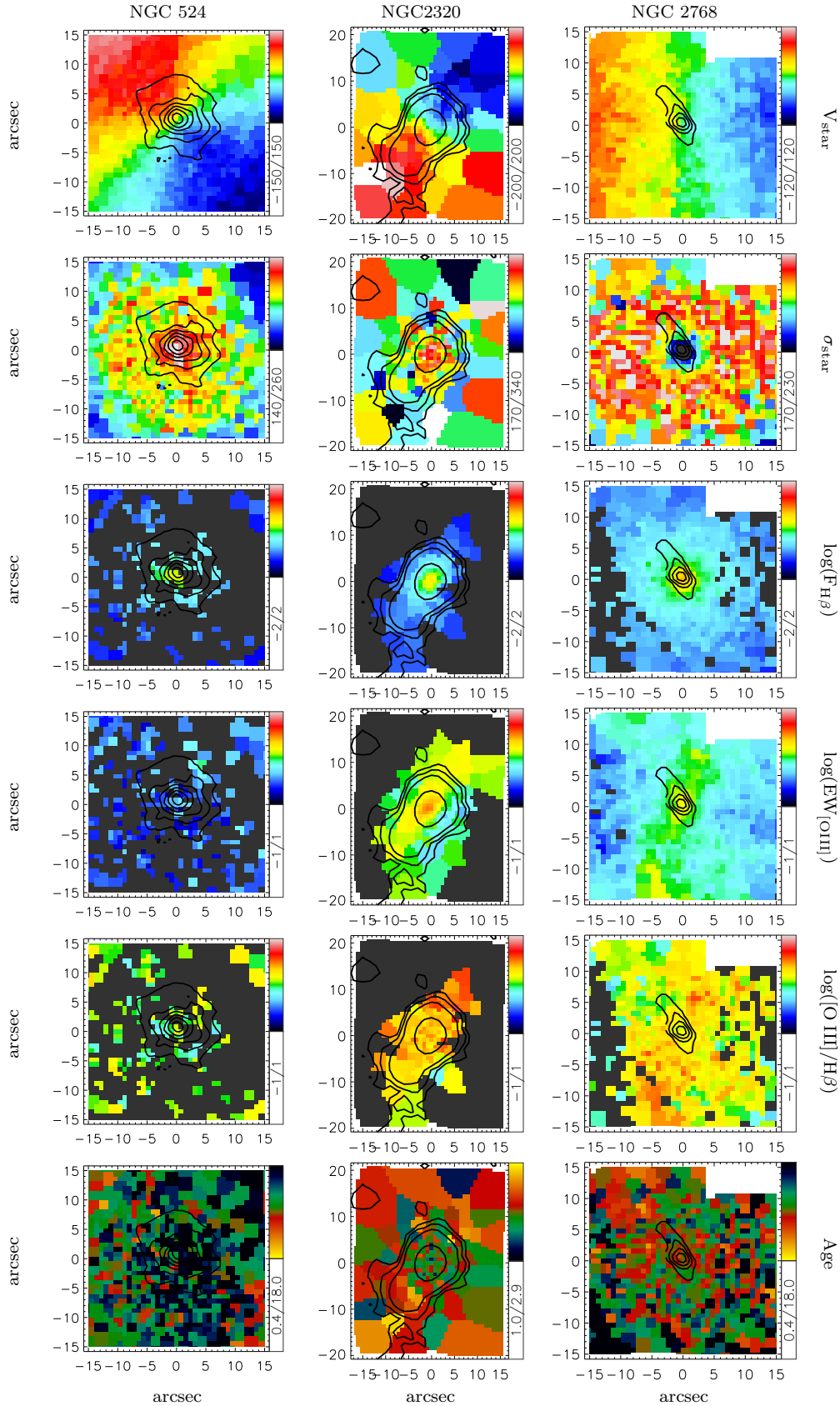
Figure 6. CO contours overlaid on IFU maps. *Top to bottom:* mean stellar velocity (km s^{-1}), stellar velocity dispersion (km s^{-1}), logarithmic Hβ emission line flux (10^{-16} erg s^{-1} cm^{-2} arcsec^{-2}), logarithmic equivalent width of [O III] (Å), logarithmic [O III]/Hβ emission line ratio, SSP-equivalent age (Gyr; except for NGC 2320 and NGC 5666 where the Hβ absorption linestrength is shown in Å).
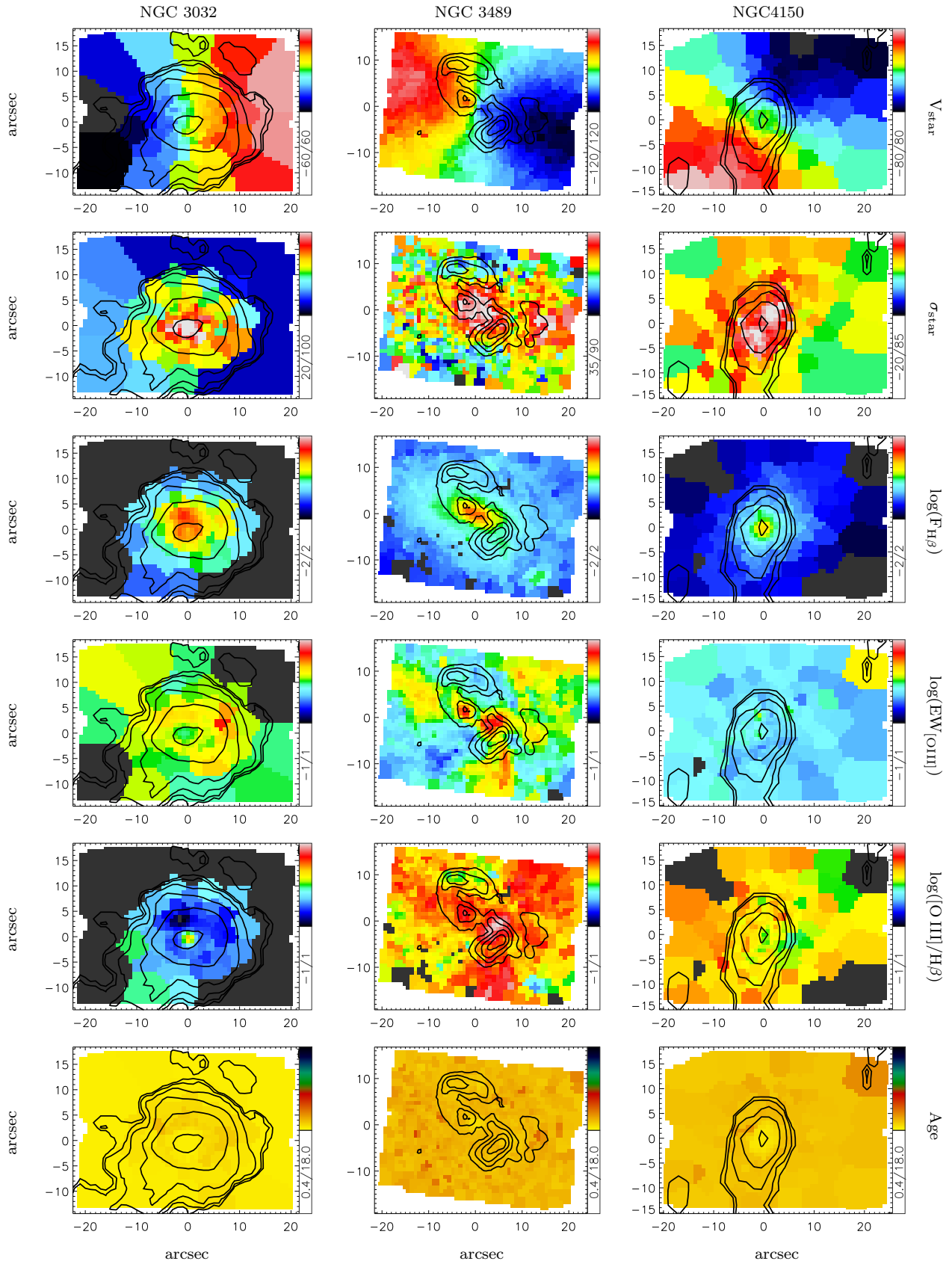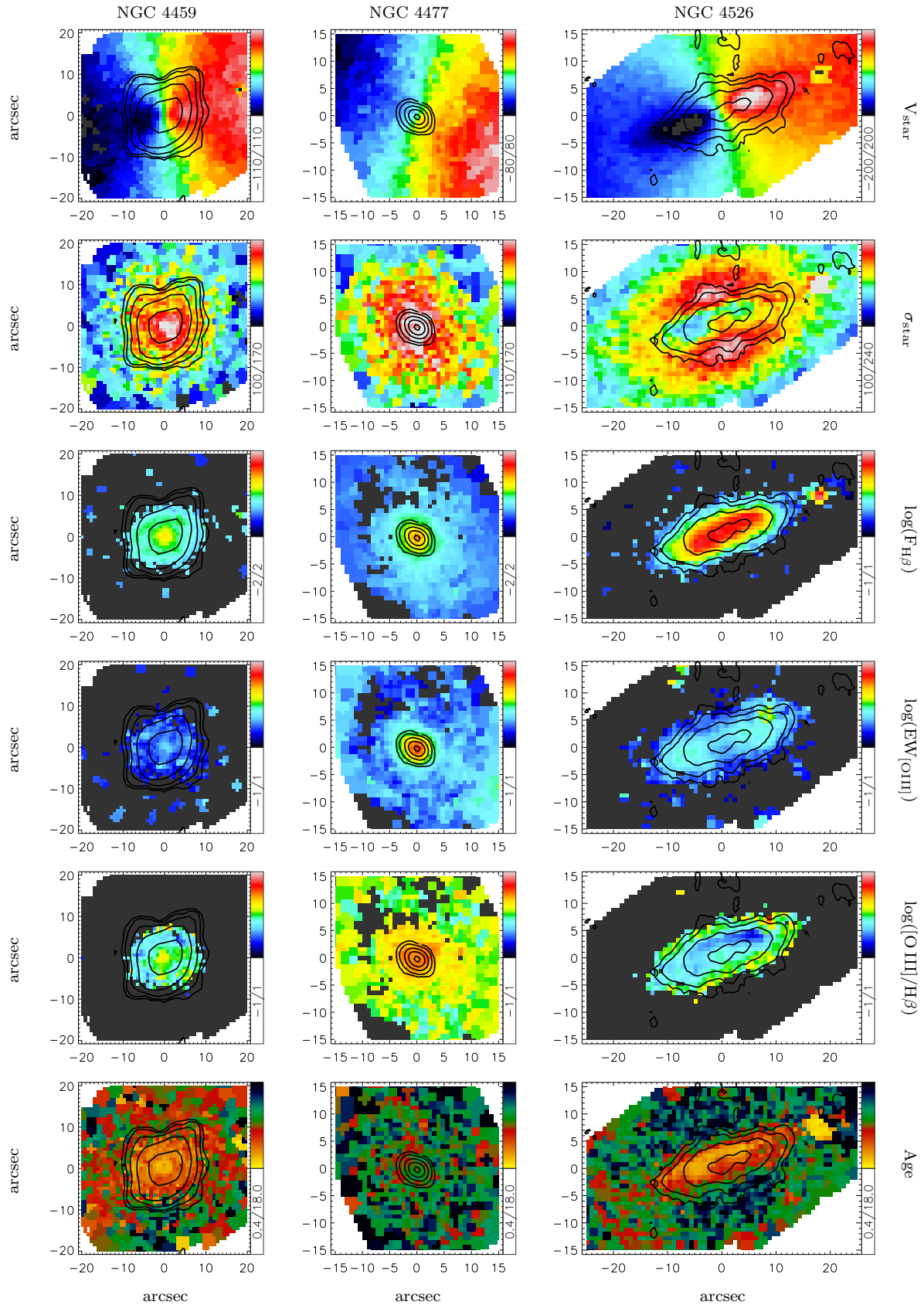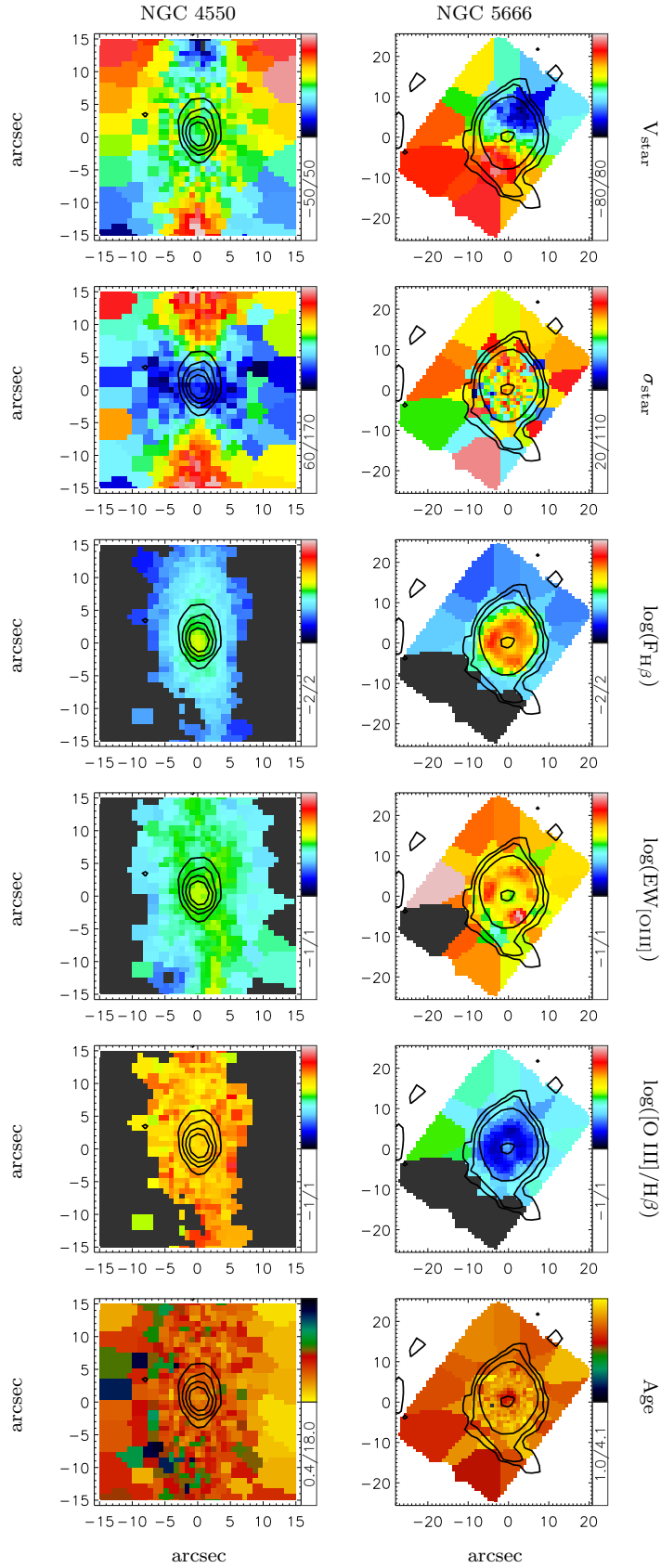
Figure 6 – *continued*

Figure 6 – *continued*

NGC 4550

NGC 5666

Figure 6 – *continued*

Table 5. Ionisation and stellar population properties

Galaxy	Ion. Source	[O III]/Hβ	$(B - V)_e$	Age$_{NUV-V}$	Hβ (R$_e$/8)
NGC 524	star-formation(?)	0.00	1.07	old	1.34
NGC 2320	young pAGBs, AGN	0.36	0.87	—	1.80
NGC 2685	young pAGBs	0.28	0.94	—	1.99
NGC 2768	old pAGBs, AGN	0.26	0.96	old	1.68
NGC 3032	star formation	-0.41	0.63	young	4.77
NGC 3156	young pAGBs	0.39	0.77	—	4.44
NGC 3489	young pAGBs	0.57	0.85	—	2.81
NGC 4150	young pAGBs	0.19	0.83	young	3.53
NGC 4459	star-formation	-0.07	0.97	young	2.14
NGC 4477	old pAGBs, AGN	0.34	0.97	old	1.62
NGC 4526	star formation	-0.20	0.98	young	1.84
NGC 4550	young pAGBs	0.36	0.89	young	2.04
NGC 5666	star-formation	-0.63	0.86	—	3.47

NOTES FOR COLUMNS: (2) based on Sarzi et al. (2006), (3) integrated total [O III]/Hβ ratio, (4) from HyperLeda database, (5) based on Jeong et al. (2009), (5) from Kuntschner et al. (2010).
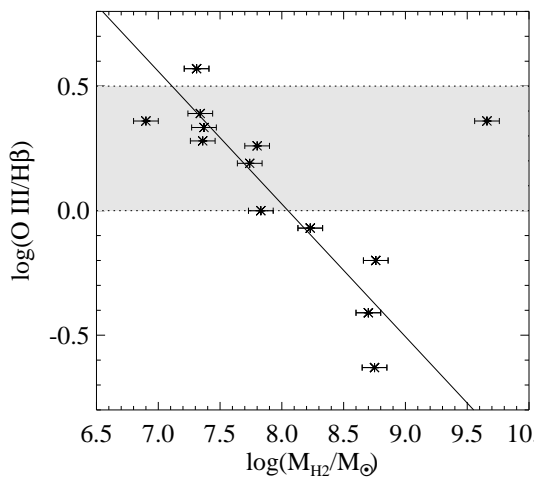

Figure 7. Total integrated [O III]/Hβ ratios from Sarzi et al. (2010) data as a function of molecular gas mass. Galaxies with more molecular gas have correspondingly lower [O III]/Hβ ratios, with higher ratios for galaxies with less molecular gas. The one exception is NGC 2320, which has a very high [O III]/Hβ ratio despite having the most molecular gas of our E/S0 sample. The solid line represents a regression to all the galaxies except NGC 2320. The shaded region represents the area with [O III]/Hβ values found for SAURON galaxies without any molecular gas.

Figure 8. Colour-magnitude diagram. Blue circles represent the early-type galaxies with molecular gas in our sample. Red diamonds are the SAURON sample E/S0s without molecular gas. Small cyan and orange circles represent late-type and early-type galaxies from HyperLEDA, respectively. From left to right, the two unlabelled galaxies are NGC 4459 and NGC 4477.

in our sample of E/S0s with molecular gas. However, this ionised gas is only ionised by star formation in 5 galaxies. In the other galaxies (mostly with less molecular gas), other ionisation sources dominate, such as young and/or old pAGB stars and AGN.

5.3   Molecular gas and stellar populations

Because they contain molecular gas, we expect our sample galaxies to host young stellar populations. Here we investigate the presence of such young populations using optical and UV colours and absorption linestrengths.

A first check for young stars can be made with optical colours. To do this, we plot a colour-magnitude diagram
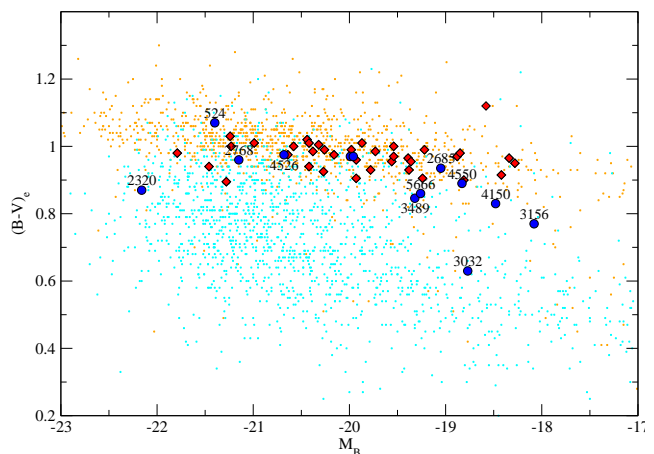
using $(B - V)_e$[1] colour against absolute blue magnitude (Fig. 8). Our sample galaxies are shown as blue circles, while SAURON galaxies without molecular gas are shown as red diamonds. Other late-type (t > 1) and early-type (t < -1) galaxies are shown as small cyan and orange points, respectively. The SAURON galaxies without molecular gas lie on the colour-magnitude relation characteristic of most early-type galaxies, i.e. the red sequence. While some of our sample galaxies also lie on this red sequence, about half are bluer, a property presumably attributable to their hosting a significant fraction of young stars.

However, optical colours are not very sensitive to young stellar populations and the UV provides a distinct improve-

---

[1] $(B - V)_e$ is the $B - V$ colour within the aperture that contains half of the total B-band flux. Values are from the HyperLEDA database (http://leda.univ-lyon1.fr) and are listed in Table 5.

ment (e.g. Schawinski et al. 2007b). Based on Jeong et al. (2009), 5/8 of our sample galaxies with GALEX (Galaxy Evolution Explorer) UV imaging data contain blue NUV−V colours indicative of a young stellar population (see Table 5, while this fraction is only 4/26 for the rest of the SAURON sample. Of the five sample galaxies with young NUV−V colours, two are on the optical red-sequence, confirming the greater sensitivity of the UV to young stars. However, the other three sample galaxies with GALEX data show no sign of a young stellar population in the UV. As for the four galaxies with blue NUV−V colours from the non-CO detected SAURON sample, three have such blue colours only at large radii, outside of the central area searched for CO. Either there is molecular gas and star formation at these large radii, or young blue stars have been recently accreted from a satellite. The fourth galaxy is NGC 7457, for which we have documented a firm CO upper limit. It seems to be a post-starburst galaxy that has evacuated all its molecular gas. Thus there is a strong, but not one-to-one, link between central blue NUV−V colours and the presence of molecular gas in early-type galaxies.

Absorption linestrengths obtained from the IFU data can also be used to estimate the ages of the stellar populations and helpfully provide information about the spatial distribution of the young stars. The measured linestrengths (see Table 5) are used in combination with theoretical models for SSPs to determine the age, metallicity and [α/Fe] ratio of a galaxy. Fits to these parameters for the SAURON galaxies are presented in Kuntschner et al. (2010). We show CO distributions over age maps in Fig. 6, except for the two galaxies outside of the SAURON sample, NGC 2320 and NGC 5666. For these two galaxies, we show the CO distributions over the Hβ linestrength maps instead, as Hβ is the most age-sensitive linestrength measured.

The CO contours over the age maps reveal various relative distributions of young stars and molecular gas. Four galaxies have globally young (< 3 Gyr) SSP ages, extending beyond the region of detected molecular gas, while two galaxies have extended intermediate (3-7 Gyr) SSP ages. In two other galaxies, a distinct change from intermediate to old SSP age occurs exactly at the boundary of the detected molecular gas. Because the SSP fit tries to account for both a young and old population in a single age, the age derived partly reflects the age of the young population and partly the fraction of young to old stars. Since all of these galaxies are likely forming some stars from their molecular gas, the intermediate ages found in some of the galaxies probably reflect lower mass fractions of truly young stars. However, three sample galaxies also have purely old populations based on their SSP fits. These are the same galaxies that have purely red NUV−V colours. Using a central ($R_e/8$) age of 5 Gyr to divide young and old galaxies, around 55% of galaxies with molecular gas have young SSPs and only 11% of those without molecular gas. If a SSP age of 2 Gyr is used instead, these percentages change to 36 and 0%, respectively.

The optical colours, UV-optical colours and the SSP-equivalent age maps described above trigger two interesting questions. Firstly, why do some galaxies have no sign of a young stellar population despite having molecular gas? Secondly, why are the young stellar populations in four galaxies so much more extended than the molecular gas we observe?

Three sample galaxies have predominantly old stellar

Table 6. Molecular to stellar mass ratios

SSP Age	NGC	$(\frac{M}{L})_{\rm Jeans}$ $(\frac{M_\odot}{L_{\odot,I}})$	$\log(M_*)$ (M$_\odot$)	$\log(\frac{M_{\rm H2}}{M_*})$	$f_{\rm YC}$ (%)
Old	524	5.04	11.2	-3.4	0.02
	2768	5.32	10.7	-2.9	0.05
	4477	3.22	10.4	-3.1	0.09
Young	3032	1.40	10.3	-1.5	2.88
	3489	0.99	10.2	-2.9	0.21
	4150	1.56	10.0	-2.2	0.32
	4459	2.76	10.8	-2.6	0.13
	4526	3.51	10.3	-2.4	0.18
	4550	2.81	10.0	-3.1	0.06
	5666	1.40	10.5	-1.8	4.71

NOTE: $(\frac{M}{L})_{\rm Jeans}$ is the mass-to-light ratio derived from the Jeans models of Cappellari et al. (2006) or Scott et al. (2009). M_* is the stellar mass within the region with detected CO. $\frac{M_{\rm H2}}{M_*}$ is the ratio of molecular gas to stellar mass within the region with detected CO. $f_{\rm YC}$ is the expected mass fraction of young to old stars based on the current SFR extrapolated over the past 1 Gyr.

populations: NGC 524, NGC 2768 and NGC 4477. One possibility is that the young populations in these galaxies are simply too small relative to the old population to be detected. To test this hypothesis, we have calculated the stellar mass contained within the region of detected molecular gas for each sample galaxy, using I-band images from the MDM observatory (Falcón-Barroso et al., in prep). This mass is listed in Table 6, along with the ratio of molecular gas to stellar mass and the expected percentage of young stars given an extrapolation of the current SFR over the past 1 Gyr (SFRs taken from Table 8 with the following order of preference: Hα+PAH, Hα+24μm, Hα+TIR). We also note the mass-to-light ratios used, which are based upon the Jeans models of Cappellari et al. (2006) and Scott et al. (2009). For galaxies not in either of these papers, we use an average-age mass-to-light ratio from galaxies with similar absorption linestrengths, which should capture the first-order effects of different stellar populations.

This calculation shows that the galaxies without detected young stars have some of the lowest molecular gas to stellar mass ratios and predicted young star mass fractions. It is difficult for both UV colours and absorption linestrengths to detect young stellar populations of less than about 0.1% in mass. Our three purely old galaxies are all below this limit. However, several galaxies with detected young stars have only slightly higher fractions. Whether a galaxy has a detectable fraction of young stars may thus be due more to peculiarities in its recent star formation history - either star formation is just starting or has been less efficient than assumed in the purely old galaxies, or star formation has recently been more vigorous in the others. This calculation of the molecular gas to stellar mass ratio shows that the old ages found for some galaxies indicate very low ratios of young to old stellar populations, but they do not completely rule out the presence of young stars.

Four sample galaxies have young stellar populations (< 3 Gyr) more spatially extended than their molecular gas (NGC 3032, NGC 3489, NGC 4150, NGC 5666). They do not show a distinct change in stellar population at the molecular gas boundary; instead each has a smooth age gradient, with younger stellar populations toward the centre where

the molecular gas lies. The age gradients combined with the spatially limited molecular gas suggests that star formation has ended at larger radii first and is ceasing in an outside-in manner, a possibility first suggested by Shapiro et al. (2010) for these same galaxies based on the spatial distribution of polycyclic aromatic hydrocarbon (PAH) containing dust. The exhaustion of the gas supply through star formation could explain such a radial trend, as could the enhanced removal of outer gas from ram-pressure or dynamical stripping. AGN feedback cannot be invoked for these galaxies, as an AGN would presumably disrupt the inner gas first. Additionally, no clear sign of AGN activity is seen. These four galaxies with extended young stellar populations all lie below the optical red sequence at the low-mass end of our sample distribution and should join the red sequence soon as their star formation continues to decline. However, we note that the same process, if present in more massive galaxies, may be hidden by their dominant old stellar populations.

In short, the comparison of the molecular gas content and extent shows that young populations and molecular gas are closely related, but not uniquely. Some galaxies with molecular gas do not show signs of a young stellar population (likely because the old population dominates) and a small proportion of galaxies without any detected molecular gas do have young stars. In a handful of our sample galaxies, we see evidence that star formation ceased at large radii before the inner radii where the molecular gas is currently located.

5.4   Molecular gas and stellar kinematics

Stars recently formed from a molecular gas disc or ring will have discy kinematics, dominated by high rotation and low velocity dispersion. If these disc stars contribute enough to a galaxy's light, we should see this contribution in the mean stellar velocity and velocity dispersion fields, with some dependence on inclination. Maps of these quantities with overlays of molecular gas contours are shown in Fig. 6 for all of our sample galaxies.

Four galaxies (NGC 3489, NGC 4459, NGC 4526 and NGC 5666) show discy stellar components related to the CO. Additionally, in one galaxy (NGC 3032), such a component is detected in a higher-resolution stellar velocity map from McDermid et al. (2006). The remaining galaxies have no stellar kinematic feature directly attributable to the molecular gas via star formation, although peculiar features which most likely indicate past interactions are visible in three galaxies (see Crocker et al. 2008, 2009; Young et al. 2008 for discussions). In general, it is thus the galaxies with clear young stellar populations that show signs of a related cold kinematic component, while galaxies with intermediate and old SSP ages do not. This bimodality is as expected since both properties depend on the light from young stars dominating that from old stars.

5.5   A classification

Some early-type galaxies have detectable young stellar populations, while others do not. Similarly, some have their ionisation dominated by star formation while others do not. Fig. 9 illustrates where galaxies lie with regards to their Hβ absorption linestrength within $R_e/8$ from Kuntschner et al.
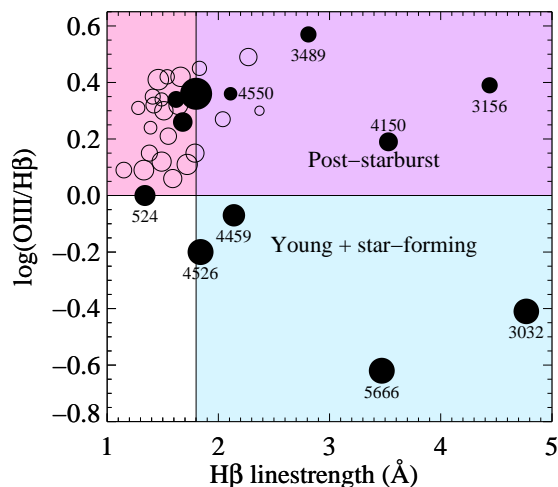

Figure 9. A loose classification for E/S0s with molecular gas based on the total integrated [O III]/Hβ emission and the Hβ absorption linestrength within $R_e/8$. Galaxies detected in CO are shown as filled black circles while those undetected in CO are shown hollow. Three regions are inhabited by our sample galaxies. In the blue region are galaxies whose gas ionisation is currently dominated by star formation, also showing either locally or globally young stellar populations (only galaxies with CO). In purple are probable post-starburst galaxies, which have young stellar populations but whose ionisation is not currently dominated by star formation (both with and without CO). In pink are galaxies whose gas is not ionised by star formation, nor do they display young stellar populations (mostly galaxies without CO). The size of the symbols logarithmically scales with the molecular gas mass (or mass upper limit) in each galaxy.

(2010) and their total integrated log([O III]/Hβ) in emission from data from Sarzi et al. (2010). The sample CO-detected galaxies are shown as filled circles whose size is proportional to the logarithm of their molecular gas mass. SAURON sample galaxies not detected in CO are shown as hollow circles with size proportional to the logarithm of their molecular mass upper limit. (Some galaxies without CO are also undetected in ionised gas and are not shown at all.)

The galaxies without detected molecular gas inhabit a relatively limited region of this diagram. All have a log([O III]/Hβ) ratio above 0.0 and most have old populations indicated by a Hβ linestrength value less than 1.8 Å. These boundaries are motivated by the expectation of ionisation only from star formation at log([O III]/Hβ) < 0.0 and the definite presence of a young stellar population when the Hβ linestrength > 1.8 Å (this choice of limit also agrees with the NUV$-V$ criterion in Jeong et al. 2009). Only around 14% of the galaxies with ionised gas but no detected molecular gas have young stellar populations. These galaxies have probably undergone an episode of star formation in the recent past but have little or no remaining molecular gas.

Galaxies with molecular gas are spread fairly equally between 3 different categories: those that are young and strongly star-forming, those that are young but whose ionisation is not currently dominated by star formation, and those that appear old and not star-forming, similar to the majority of galaxies without molecular gas. The galaxies in the young and star-forming region all have over 10^8 M$_\odot$

Table 7. Accretion signs

NGC	PA_g-$PA_\star$ (deg)	$\log(M_{HI})$ ($M_\odot$)	H I Morphology	H I Ref.
524	1	6.41	distant cloud	1
2320	≈ 0	< 7.75	—	2
2685	73	9.26	warped polar disc	3
2768	-95	8.23	central cloud; tail	3
3032	-151	7.98	central disc	1
3489	-6	6.76	central disc; tail	1
4150	21	6.40	central disc; tail	3
4459	-1	< 6.59	—	1
4477	-28	< 6.61	—	1
4526	6	< 7.88	—	4
4550	0	< 6.57	—	1
5666	≈ 0	9.23	extended disc	1

NOTES: PA_g-$PA_\star$ is the difference between the ionised gas and stellar kinematic position angle from Sarzi et al. (2006), except for NGC 2320 and NGC 5666 where it is estimated by eye to be close to zero (definitely co-rotating). H I references: (1) Oosterloo et al. (in preparation), (2) Lucero & Young (2008), (3) Morganti et al. (2006), (4) di Serego Alighieri et al. (2007).

of molecular gas and have the highest star formation rates (see Table 8). Galaxies in the second category have young stellar populations but high [O III]/Hβ ratios probably due to young pAGB stars. All have less than 10^8 M$_\odot$ of H$_2$, including some that have not been detected with CO. The apparently old and not star-forming galaxies with molecular gas have received attention previously in Section 5.3. These galaxies may be star-forming, but the amount of star formation relative to their old stellar mass is not sufficient to make the young stars detectable. They thus appear similar to galaxies that do not contain molecular gas.

In general, we expect galaxies to cycle through this diagram as they acquire, use and then exhaust a supply of cold gas. Consider a quiescent early-type galaxy that accretes a significant amount of gas. First, we expect it to move down from the old region as star formation starts to dominate the ionisation and the [O III]/Hβ ratio thus drops. When the young stars become a significant mass fraction of the old stellar population, the Hβ linestrength will increase, moving the galaxy into the young and star-forming region in Fig. 9. The galaxy may remain there star-forming for some time, but eventually it will start to exhaust its gas supply and its SFR will decline. Then young pAGB stars will start to dominate the ionisation and the galaxy will move up to the 'post-starburst' region of the diagram, even if it is still moderately star-forming. As the SFR continues to decline and then stops, the young stars will be less important relative to the old stars and the Hβ linestrength will decrease, eventually reaching values consistent with a purely old population.

6 DISCUSSION

6.1 Origin of the gas

The cold gas in early-type galaxies is probably either accreted from an external source or results from internal stellar mass loss. For some galaxies, cold gas may also remain from before the morphological transition to early-type (i.e. from their presumed spiral progenitors). These scenarios are dif-

ficult to distinguish, but the kinematic misalignment of gas and stars or a disturbed atomic hydrogen distribution are telltale signs of external accretion.

As ionised gas in our sample galaxies always seems kinematically linked with the molecular gas and its kinematic position angle is more reliably determined, we use here the difference in kinematic position angles between the ionised gas and stars from Sarzi et al. (2006), listed in Table 7. In 8/12 galaxies, the gas rotates in the same direction as the stars and thus may be contributed by either internal or external processes. However, the polar rotating gas in NGC 2685 and NGC 2768 and the counter-rotating gas in NGC 3032 must have been contributed by external sources. In NGC 4550, the gas most likely remains from a merger of two disc galaxies (Crocker et al. 2009).

About half the sample galaxies are also detected in H I. Out of the six firmly-detected galaxies, three show signs of possible ongoing accretion. The case is most clear for NGC 2768, that has a small amount of H I at the galaxy centre, but a distinct and massive tail of H I extending toward the northeast (Morganti et al. 2006). Crocker et al. (2008) discuss possible accretion scenarios for this galaxy in detail, suggesting that a nearby spiral galaxy is the most likely donor of the gas. NGC 3489 and NGC 4150 both have very low column density tails of atomic hydrogen (Oosterloo et al. in preparation) that indicate ongoing accretion. However, neither of these galaxies has much additional cold gas to accrete.

Thus out of our sample, three galaxies must have acquired their gas externally, as indicated by gas misalignment, and two more show hints of ongoing accretion. All of these galaxies with recent or ongoing accretion are located in the field, hinting at the difficulty of gas exchange when a hot intracluster medium is present. These five galaxies are a lower limit to the incidence of accretion; in others, the obvious signs of accretion may have already disappeared. In NGC 4550, gas appears to have been contributed along with stars in a major merger, potentially the merger that transformed it to an early-type galaxy. But internal stellar mass loss may also be important for the other galaxies, especially those in a cluster environment.

6.2 Star formation tracers

Early-type galaxies provide unique conditions to study star formation, with their deep potential wells, hot gaseous halos, relatively little cold gas, frequent AGN and only weak, if present, stellar discs. Considering these physical differences, we are interested in whether the molecular gas in early-type galaxies forms stars in the same manner as in spirals. To do this, we must reliably estimate the star formation rate. Multiple potential tracers exist: radio continuum (synchrotron emission from supernova remnants and thermal emission from H II regions), mid-infrared (MIR) and FIR emission (produced by young stars heating their dusty environs, i.e. obscured star formation), Balmer line emission (by young stars ionising surrounding gas) and UV radiation (unobscured young O and B stars). Each of these tracers is used as a SFR measure in the literature (see Kennicutt 1998a for a review).

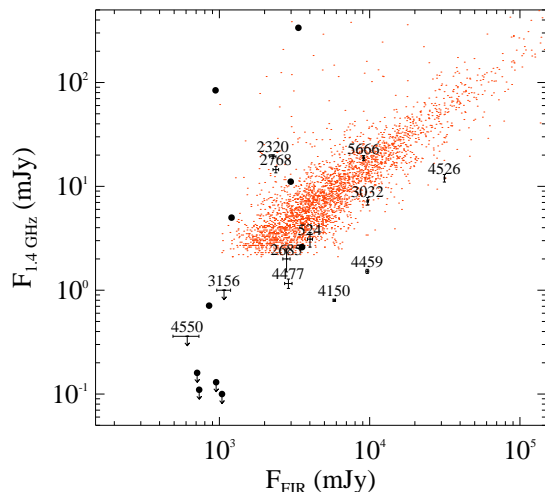All of these tracer-SFR conversions, however, rely on star formation and directly related processes being the dom-

Figure 10. Radio continuum versus FIR flux. The UGC sample from Condon et al. (2002) is shown as red points. Our sample galaxies are shown with black error bars, while SAURON sample E/S0s without detected molecular gas are filled black circles.

inant source of the observed emission. In early-type galaxies, this may not always be the case. For example, MIR and FIR emission is present in early-type galaxies that are clearly quiescent (Temi et al. 2007), as is extended Hβ emission (Sarzi et al. 2006). Radio AGN can contribute significantly to radio emission and some old stars emit in the UV (the UV-upturn phenomenon; see e. g. O'Connell 1999 for a review). By comparing their fluxes, we will investigate here the reliability of radio, FIR and Hβ emission as star formation tracers in early-type galaxies. If two of these measures accurately trace star formation, a linear relation should hold between them. The use of 8 and 24μm emission as star formation tracers for the SAURON sample is discussed in Shapiro et al. (2010) and Temi et al. (2009a), respectively. The UV is treated in Jeong et al. (2009), but traces young stellar populations better than it does the current star formation rate.

6.2.1 Radio-FIR correlation

The tight relation of radio continuum and FIR fluxes in star-forming galaxies holds over five orders of magnitude (Price & Duric 1992). This relation is attributed to both the FIR and radio emission tracing the current star formation rate. Star formation-associated FIR emission is produced when hot young stars heat their dusty environments. Radio emission is linked to the SFR through the release of cosmic rays by supernovae. These cosmic rays are then accelerated in the magnetic field of the galaxy, producing synchrotron radiation. However, the relation is slightly non-linear below $L_{\mathrm{FIR}} < 10^9$ L$_\odot$. Weaker FIR galaxies have either radio deficits or FIR excesses with respect to higher FIR galaxies (Yun et al. 2001).

To compare the radio and FIR emission we plot the radio flux against the FIR flux in Fig. 10. The small red points represent the Condon et al. (2002) sample of NRAO VLA Sky Survey (NVSS) and IRAS detected galaxies from the Uppsala General Catalogue (UGC). The UGC cata-

logue contains both spiral and early-type galaxies, although many early-type galaxies are not detected and most that are detected are radio AGN. Our sample of CO-detected E/S0 galaxies is overplotted with error bars and marked with each galaxy's NGC number. We also plot the few (10) SAURON sample galaxies without CO that are detected by IRAS (filled circles). Fig. 10 shows that early-type galaxies do not follow the star-forming relation, even those with molecular gas. The E/S0s with molecular gas are primarily below (FIR-excess or radio deficient) the star-forming relation, aside from two galaxies hosting radio AGN (NGC 2320 and NGC 2768) and NGC 5666.

The mismatch between early-type galaxies and the radio-FIR correlation was first thoroughly presented in Walsh et al. (1989), although they had no external way to separate galaxies likely to be star-forming. Lucero & Young (2007) discuss the radio-FIR correlation for a sample of 6 early-types with molecular gas (thus likely star-formers) and find that most lie close to the radio-FIR relation, although half are below, similar to what we find. Results on spirals from Condon et al. (1991) also indicate that more FIR or less radio emission is found for earlier types (Sa-type spirals). They offer a simple model to explain this change of ratio, based on lower-mass stars (which will not produce supernovae) contributing significantly to the dust heating in these galaxies. Our work in Section 6.2.4 also shows a FIR-excess with respect to the 8 and 24μm emission, further supporting the low-mass star heating explanation. However, a handful of galaxies are extremely deviant, lying a factor 10 below the relation (NGC 4150, NGC 4459 and NGC 4550). The FIR excess with respect to the mid-IR is not strong enough to explain this large offset, and it is possible another cause (more efficient cosmic ray escape or weak magnetic fields) is also at work. Four galaxies without CO, but with IRAS detections, also lie far below the radio-FIR relation. These are possibly false IRAS detections, as they are right at the detection limit. Otherwise, they may host a small quantity of dust, heated by old stars, without any recent supernovae to provide the cosmic rays necessary to produce the radio synchrotron emission.

The poor relation between the FIR and radio emission in early-type galaxies with molecular gas warns of a flaw in one or both of these tracers as a star formation rate indicator.

6.2.2 Hβ as a star formation tracer

If Hα emission is corrected for dust extinction, the FIR and Hα emission are proportional over four orders of magnitude in star-forming galaxies (Kewley et al. 2002). Unfortunately, the SAURON wavelength range only includes the weaker and more dust-extincted Hβ emission line. Even in clearly star-forming galaxies, Hβ does not trace star formation, as can be seen in the top two plots of Fig. 11. These plots show no correlation between Hβ and either the FIR or radio flux for the galaxies of the Near Field Galaxy Survey (NFGS) sample, a local field galaxy-only sample that is comprised mostly of star-forming galaxies (Jansen et al. 2000). However, when these same galaxies are extinction-corrected based on the Balmer decrement between Hα and Hβ, a strong correlation between extinction-corrected Hα and FIR is present, and a slightly weaker correlation is observed between the cor-
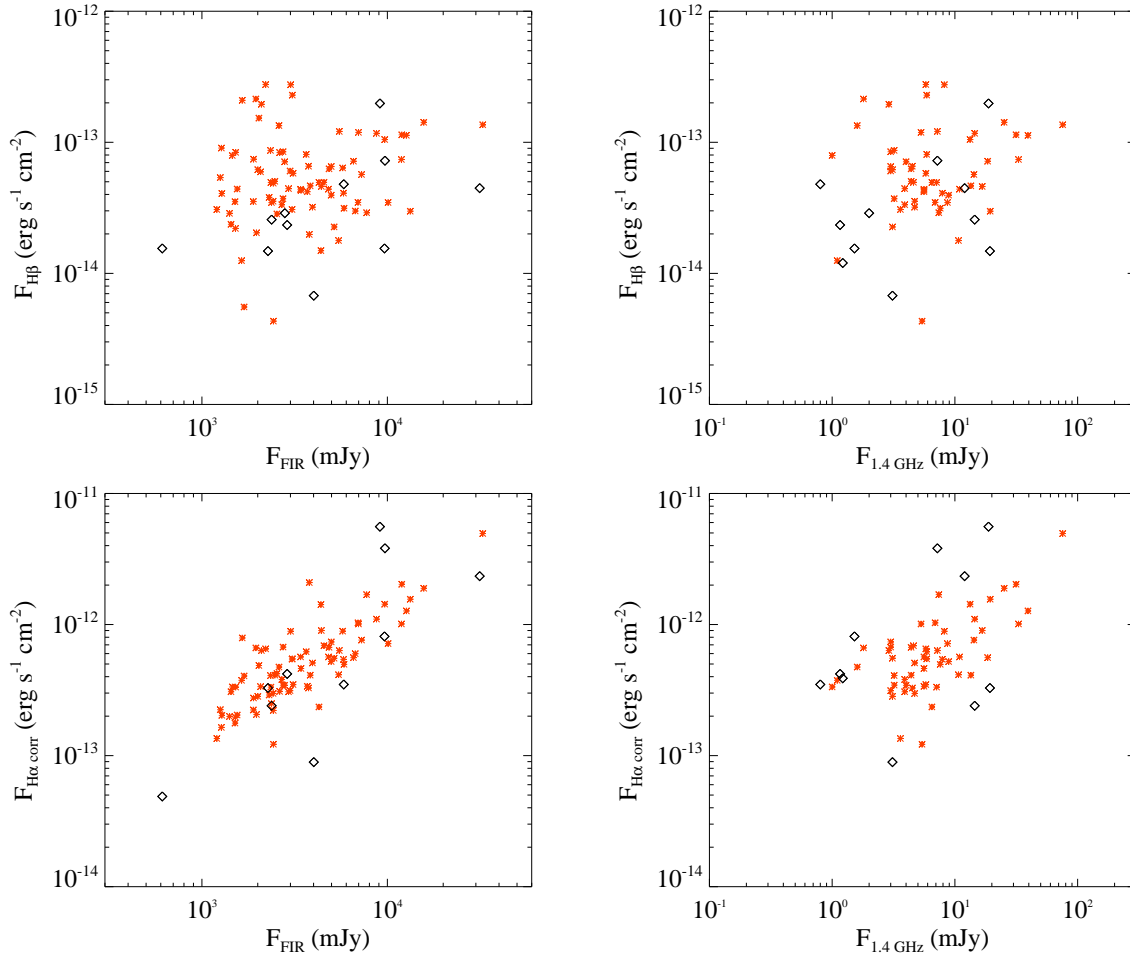
Figure 11. *Top-left:* Hβ flux versus FIR flux. *Top-right:* Hβ flux versus 1.4 GHz continuum flux. *Bottom-left:* Extinction-corrected Hα flux versus FIR flux. *Bottom-right:* Extinction-corrected Hα flux versus 1.4 GHz continuum flux. Red asterisks represent galaxies from the NFGS sample, while our E/S0s with molecular gas are shown as black diamonds. Correlations are not seen with the Hβ emission either in our sample or the NFGS galaxies, while correlations are clearly observed with extinction-corrected Hα in the NFGS and probably for our sample E/S0s as well.

rected Hα and radio emission (bottom of Fig. 11; Kewley et al. 2002).

Without observed Hα emission, we cannot perform the same simple extinction correction for the SAURON galaxies. Instead, we assume an extinction to hydrogen column density ratio and use our molecular gas maps along with HI data to estimate the extinction in each pixel of the Hβ flux maps. Summing over the region with detected molecular gas then gives us the corrected Hβ flux associated with the region where star formation is expected. The details of this process are as follows. First, we calculate the H_2 column density using the same X_{CO} factor, 3.0×10^{20} cm^{-2} (K km s^{-1})$^{-1}$, used to calculate the total molecular masses. As the HI maps are at much lower spatial resolutions, we calculate the average central HI to H_2 mass ratio for each galaxy and multiply the H_2 column density by this factor to estimate the column density of HI. If no HI is detected for a galaxy, we assume no HI is present. We then add the H_2 and HI column densities and divide by the mass of a hydrogen atom to get the number column density of all hydrogen atoms in cm^{-2}. We note that including the HI is a 10% or less addition

for all galaxies (except NGC 5666, where it is 30%). However, only a portion of the gas and dust is actually in front of the line-emitting gas. A first order approximation is that half of the dust is in front (see Appendix 1 of Calzetti et al. 2007). The colour excess is based on the Milky Way-derived relation: $E_{B-V} = 1.7 \times 10^{-22}$ cm^2 $n(H)$ (Bohlin, Savage & Drake 1978). We also assume a Milky Way total-to-selective extinction ratio of $R_V = 3.1$ and then use the Cardelli et al. (1989) extinction curve to calculate an extinction-corrected Hβ flux.

In some galaxies, the local estimated V-band extinction, A_V, reaches extremely high values (over 20). Any emission actually detected in Hβ is unlikely to have originated in regions with such high extinctions, instead what we observe must come from outer layers with less extinction. Using such high A_V values produces unrealistically high estimates for the corrected Hα emission (calculated assuming a Balmer decrement of 2.86 between Hα and Hβ, as expected in the case of no reddening and Case B recombination from 1989). Instead of using these very high values, we set an upper limit of $A_V = 2.5$. This choice is motivated by at-

tempting to match the few galaxies for which we have observed Hα fluxes. There are four such galaxies: NGC 3032, NGC 3489, NGC 4459 and NGC 4526. The reported Hα flux for NGC 3489 is only 9.1×10^{-14} erg s^{-1} cm^{-2} (Kennicutt et al. 2008), which is less than 2.86 times the observed Hβ flux of 4.8×10^{-14} erg s^{-1} cm^{-2}. We thus do not use this observation. For NGC 3032 and NGC 4459, the choice of A_V=2.5 gives expected uncorrected Hα fluxes of 1.3×10^{-12} and 2.4×10^{-13} erg s^{-1} cm^{-2}, while the actual observed values are 7.7×10^{-13} and 4.1×10^{-13}, respectively. Thus, for these two galaxies, our estimate is 1.9 and 0.6 times the observed value, a good match considering all the assumptions and the differences in the observations (errors associated with this method are likely to be at least 50%). For the very edge-on galaxy NGC 4526, our method predicts a much lower Hα flux than is actually observed (Young et al. 1996). An A_V of 10.9 is implied by the difference between the observed Hα and Hβ fluxes. As this is an unreasonably high extinction (it leads to an Hα-estimated SFR of over 3000 M$_\odot$ yr^{-1}), we will use the Hα value we estimate from the Hβ flux, despite the large mismatch with the observed Hα flux.

Using these corrected Hα fluxes, the E/S0s with molecular gas seem to generally follow the Hα-FIR correlation delineated by the NFGS, although they show increased scatter (Fig. 11). Any correlation between Hα and the radio emission is weaker, although our E/S0s are not much offset from the NFGS relation, which also shows a larger scatter than the FIR-based relation. One curious feature of the E/S0 galaxies revealed by these plots is that the galaxies predominantly ionised by a mechanism other than star formation (i.e. the high [O III]/Hβ ratio galaxies) do not lie clearly off the Hα-FIR plot, as might be expected. This suggests that whatever additional sources ionise the gas also heat the dust, in a manner similar to hot young stars. To better explore these trends, direct measurements of Hα in more E/S0 galaxies are required.

6.2.3 MIR star formation tracers from the literature

Using Spitzer InfraRed Array Camera (IRAC) data, Shapiro et al. (2010) identify star-forming galaxies among the SAURON sample and derive SFRs using stellar continuum-subtracted 8μm PAH emission and the conversion from Wu et al. (2005). They identify 8 galaxies with clear signatures of star formation; 7/8 of these are in our sample (the one galaxy outside our sample is NGC 2974 that also shows evidence for outer star formation in the UV, as discussed in Section 6.1). They also identify another 5 galaxies that are likely to host star formation, including three of our sample galaxies (NGC 524, NGC 4477 and NGC 4550). These galaxies have less prominent 8μm PAH distributions and consist of galaxies in or close to the region of our 'old' category in Fig. 9, where the IFU data do not conclusively indicate young stars or ongoing star formation. Another galaxy from this 'old' category, NGC 2768, is classified by Shapiro et al. (2010) as unlikely to be star-forming, with its PAH emission instead excited by its general interstellar radiation field. The SFRs they derive range from 0.006 to 0.4 M$_\odot$ yr^{-1} across the SAURON sample.

The 24μm emission traces hot dust, either the ejected circumstellar material around hot old stars or the birth material of hot young stars. A study of the 24μm emission in the SAURON E/S0s was performed by Temi et al. (2009a) using Multiband Imaging Photometer for Spitzer (MIPS) data. They note that subtracting the old-star contribution from the 24μm is necessary before its use as a SFR indicator, and they base this subtraction on each galaxy's K-band luminosity. They then use the Calzetti et al. (2007) calibration to estimate 24μm SFRs for the SAURON E/S0s, finding SFRs between 0.02 and 0.2 M$_\odot$ yr^{-1}. Out of the 8 of our sample galaxies they consider, they identify 6 as star-forming. The two not identified as star-forming are NGC 2768 and NGC 4477, again two galaxies in our 'old' category that must have very low specific star formation rates.

6.2.4 Star formation rate comparison

For each of the SFR tracers discussed (1.4 GHz, FIR, 24μm, 8μm PAH, and Hα), there are ample different conversions to SFR in the literature. Consistency between the tracers is only guaranteed if the conversions are calibrated against the same set of sample galaxies. We thus turn to the calibrations found in Kennicutt et al. (2009, hereafter K09), which linearly combine the observed Hα emission (i.e. unobscured SF) with a measure of the dust emission (i.e. obscured SF): SFR=pSFR(Hα)+pSFR(IR) (see their eqn. 16 and table 4; here pSFR denotes a "partial" SFR). These calibrations provide consistent SFRs based on the Spitzer Infrared Nearby Galaxies Survey (SINGS) sample of star-forming galaxies.

We first compare the pSFRs for the four obscured SF tracers: 1.4 GHz, total infrared (TIR), 24μm and 8μm PAH (stellar continuum-subtracted) emission. The radio is justified as an obscured SF tracer based on the tight radio-FIR correlation. We use 1.4 GHz fluxes from the literature and 8μm stellar continuum-subtracted fluxes from Shapiro et al. (2010). For the 24μm emission, the stellar contribution is negligible for the K09 sample while it is significant for the SAURON E/S0 galaxies, as noted above. Thus we use the stellar continuum-subtracted 24μm fluxes from Temi et al. (2009a) as the input.

The TIR luminosity measures the total luminosity from 3 to 1000μm and is different from the FIR luminosity we used thus far (based on only IRAS 60 and 100μm fluxes). For the TIR used in their SFR calibrations, K09 use the formula from Dale & Helou (2002) that estimates the TIR flux based on IRAS 25, 60 and 100 μm data. Unfortunately, only four of our sample galaxies were detected at 25μm with IRAS, and these are all close to the detection limit. However, seven have 24μm fluxes from MIPS as reported in Temi et al. (2009b). For IR-bright SINGS galaxies, f(MIPS 24)/f(IRAS 25) = 0.98 ± 0.06, so we use this conversion factor to estimate the IRAS 25μm flux, adding the 0.06 error in quadrature. We note that the 24μm flux for NGC 5666 in Temi et al. (2009b) was unrealistically large and we have substituted the value reported in Young et al. (2009). We also note a possible systematic offset of around 20% in the Temi et al. (2009b) fluxes compared to IRAS 25μm fluxes for galaxies well above the detection limit in IRAS 25μm. This possible offset is likely attributable to differences in background subtraction or aperture correction. We thus use the SINGS conversion factor after subtracting the expected stellar contribution to the 24μm flux (see Temi et al. 2009a), but remain aware that the values we use for 25μm fluxes may be about 20%

Table 8. Star formation rates.

Galaxy	Partial SFRs ($M_\odot$ yr^{-1})					Total SFRs ($M_\odot$ yr^{-1})			
	TIR	24 μm	PAH	1.4 GHz	Hα	TIR+Hα	24μm +Hα	PAH+Hα	1.4 GHz+Hα
524	–	–	0.027	0.043	0.008	–	–	0.035	0.051
2320	–	–	–	3.412	0.495	–	–	–	3.908
2685	–	–	0.045	0.012	–	–	–	–	–
2768	0.041	0.006	–	0.177	0.018	0.059	0.025	–	0.195
3032	0.151	0.084	0.112	0.085	0.384	0.535	0.468	0.496	0.469
3156	0.020	0.008	0.010	–	–	–	–	–	–
3489	–	0.012	0.017	0.004	0.016	–	0.028	0.034	0.020
4150	0.032	0.014	0.017	0.004	0.013	0.045	0.027	0.030	0.017
4459	0.080	0.026	0.050	0.010	0.041	0.121	0.067	0.091	0.051
4477	–	–	0.003	0.008	0.024	–	–	0.026	0.032
4526	0.294	0.070	0.102	0.083	0.147	0.441	0.216	0.249	0.229
4550	–	–	0.002	–	0.004	–	–	0.006	–
5666	0.352	–	–	0.591	1.311	1.663	–	–	1.902

too low. We then apply the Dale & Helou (2002) IRAS-based TIR formula.

We list the consistently calculated obscured pSFRs in Table 8. Values are generally between 0.01 and 0.5 $M_\odot$ yr^{-1}. Next, we compare each obscured tracer to the others by looking at the logarithmic ratio between the two derived pSFRs. Plots showing the distribution of this ratio for our E/S0 galaxies are shown in Fig. 12 (shaded histograms). Spiral galaxies from the SINGS sample are plotted for comparison (hollow histograms). In E/S0s, the TIR consistently overestimates the SFR relative to both the 8 and 24μm tracers (top two plots of Fig. 12). This overluminosity in TIR implies a higher fraction of cold dust in early-type galaxies than in spirals. The two-component model of Lonsdale Persson & Helou (1987), in which the far-IR consists of both a star-formation related component and a component heated by old stars, suggests that the TIR will be larger relative to the SFR in galaxies with lower specific SFRs. Here we see this effect in the direct comparison of mid-IR (warm dust) and far-IR (cold dust) emission.

The ratios of 8μm PAH pSFRs to 24μm pSFRs are very similar between the SINGS spirals and the 6 E/S0s that we are able to compare (the offset of both distributions is within the error of the calibration values 'a' listed in table 4 of K09). The agreement of these tracers suggests they are the best tools for deriving SFRs for early-type galaxies. Compared to these tracers, SFRs directly derived from TIR or FIR alone may be overestimated by a factor 7 in the worst case, with an average overestimation factor of around 2.8.

The radio-derived pSFRs show a wide variation relative to all three IR-derived pSFRs. The FIR-radio has already been extensively discussed in Section 7.2.1, with one possibility for the FIR-excess or radio deficiency being an additional FIR component not associated with star formation. However, the radio pSFR is also much lower than the 24μm or 8μm derived pSFRs in 3-4 galaxies, indicating that the radio emission associated with star formation may really be deficient in these galaxies (NGC 2685, NGC 3489, NGC 4150, NGC 4459).

Next we consider the unobscured contribution (measured with Hα) to the total SFR. The pSFR from the Hα emission is similar in value to that from the IR and radio tracers (see Table 8). Fig. 13 illustrates this rough equality

- our E/S0 sample galaxies lie close to the 1-1 line when pSFR(Hα) is plotted against pSFR(IR). Note that this line is not a fit to either our or the comparison data. The different coloured points in Fig. 13 represent the different IR tracers (PAHs, 24μm and TIR) and we have also plotted galaxies from the Local Volume Legacy sample (LVL; Dale et al. 2009; Lee et al. 2009) for comparison. Many of the E/S0 galaxies with low SFRs deviate from the trend seen in the LVL galaxies. (The strong Hα and weak PAH emission of the Seyfert NGC 4477 make it the one exception.) The LVL galaxies at these low star formation rates are primarily dwarf galaxies with low metallicity and low dust content. These galaxies thus emit more in Hα (low obscuration) and less in the IR (less dust to heat). The gas phase metallicity in our E/S0s is presumably higher and thus a different trend is seen at low SFRs.

Overall, we conclude that the 8 and 24μm fluxes are the best obscured star formation tracers for early-type galaxies. The TIR leads to an overestimate because of additional dust heating by old stellar populations, and the radio continuum is easily influenced by AGN and may occasionally be deficient for as yet unknown reasons. The ratio between unobscured and obscured star formation is similar to that found in spirals, but is less than that found for galaxies of similar star formation rates from the LVL sample. This difference is probably explained by the difference in metallicity - our sample galaxies have high metallicities despite low star formation rates.

6.3 Star formation laws

Star formation laws are usually given with respect to star formation and gas surface densities and follow the form of $\Sigma(\text{SFR}) \propto \Sigma(\text{H I} + \text{H}_2)^n$. Using surface densities both removes the distance dependence of the relation and is physically motivated by theoretical predictions that star formation depends on gas volume density (e.g. Schmidt 1959). For a sample of local star-forming and starburst galaxies, Kennicutt (1998b) finds $n = 1.4 \pm 0.25$. The star formation law with this exponent is commonly referred to as the Schmidt-Kennicutt law. But other work suggests a constant star formation efficiency (SFE), in which n is nearly 1 (Young & Scoville 1991; Young et al. 1996) and a constant fraction
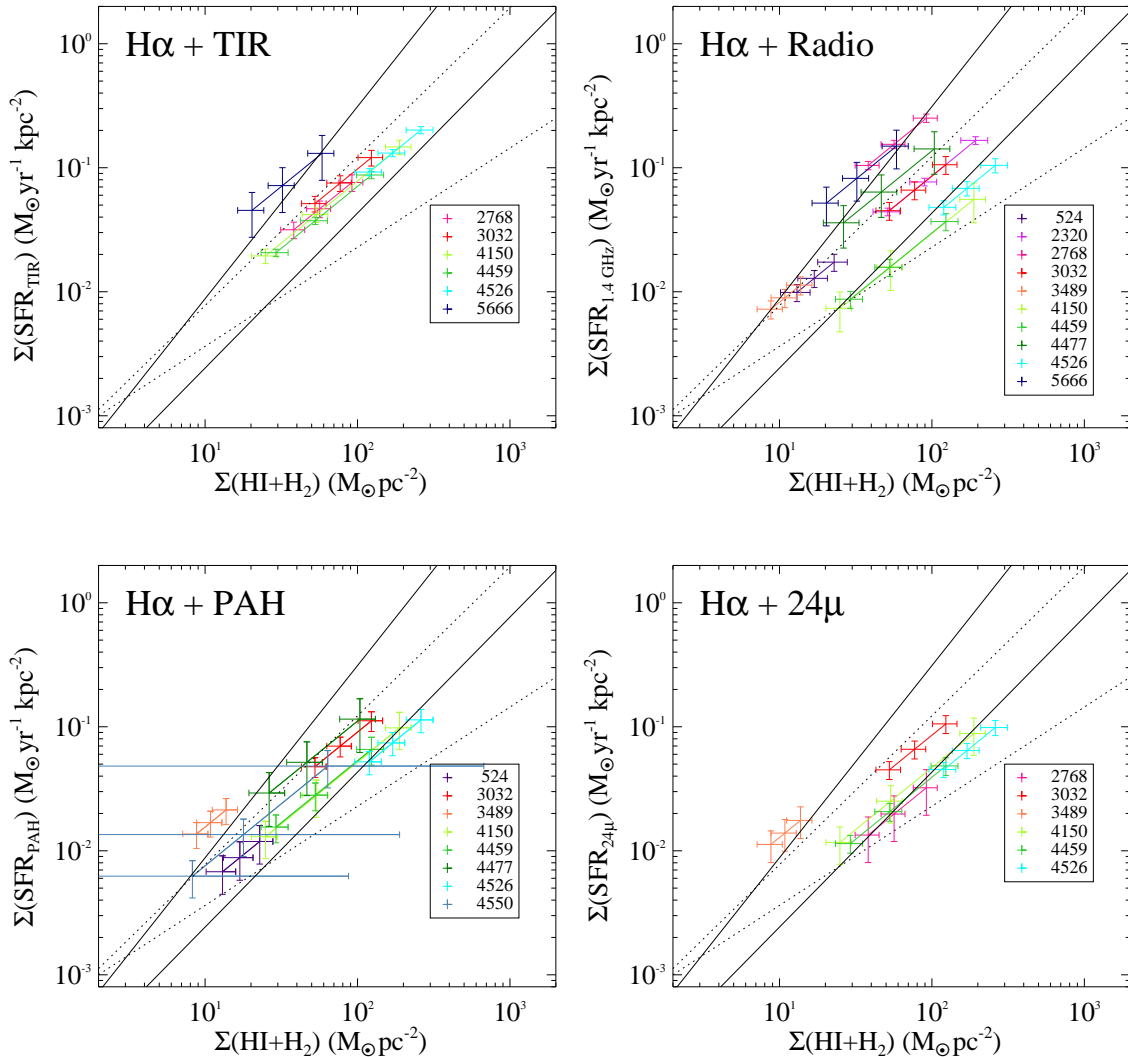
Figure 14. A total (H I + H$_2$) gas-based comparison of our galaxies with the Schmidt-Kennicutt law of Kennicutt (1998b) (solid lines) and the constant SFE prescription of Bigiel et al. (2008) (dotted lines), both updated for a Kroupa IMF and using our X$_{CO}$ factor. *Top-left:* SFR from Hα and TIR emission. *Top-right:* SFR from Hα and 1.4 GHz radio continuum emission. *Bottom-left:* SFR from Hα and 8μm PAH emission. *Bottom-right:* SFR from Hα and 24μm emission.

of gas turns into stars per unit time. For the constant SFE law, we use the prescription found in Bigiel et al. (2008). We compare our E/S0 galaxies to both the Schmidt-Kennicutt law and this constant SFE law below.

Average molecular gas surface densities are determined using the molecular gas radii R_{H_2} and H$_2$ masses. Total cold gas masses are first calculated, using the ratio of central H I (found in Morganti et al. 2006 and Oosterloo et al. in preparation) to H$_2$ mass to provide a correction factor for the H I expected within the CO radius. The CO radius is then used to calculate the average gas surface density using this total cold gas mass. We note that, as for the extinction correction in Section 7.2.2, the inclusion of H I is not a large correction. Star formation surface densities are calculated using total SFRs [pSFR(Hα) + pSFR(obscured)] and the CO radius. These total SFRs can be found in Table 8.

For each different obscured SFR tracer, we plot Σ(SFR)

against Σ(H I +H$_2$) in Fig. 14. The Schmidt-Kennicutt law given in Kennicutt (1998b) is shown via its upper and lower bounds, after having been modified for a Kroupa IMF as used in K09 (a multiplicative factor of 0.69). We also plot the constant SFE law with its bounds as described in Bigiel et al. (2008). Our sample galaxies are plotted with error bars that represent the errors in mass (for the x-axis) and SFR (for the y-axis). The errors in the radius determinations make the star formation and gas surface densities correlated such that the galaxies move along a line of slope unity for different radii. We thus represent the radius errors by plotting three different data points per galaxy: one using the measured radius, then one each using the radius plus and minus the radius error.

As seen in Fig. 14, early-type galaxies lie almost entirely within the 1σ bounds for both the Schmidt-Kennicutt and constant SFE laws (see also fig. 5 of Shapiro et al. 2010).
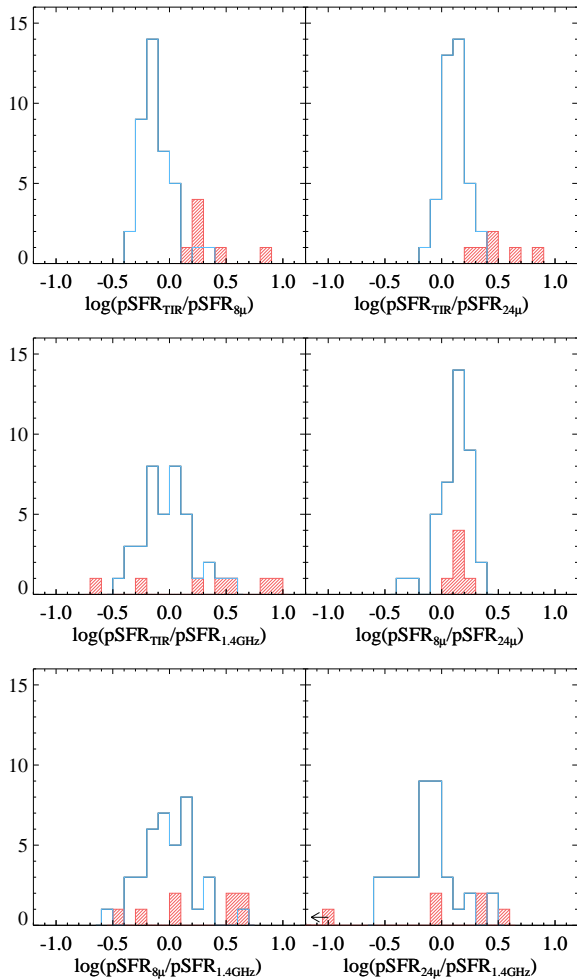
Figure 12. A comparison of obscured pSFRs derived via different tracers. The spirals from the SINGS sample are plotted in hollow histograms. The logarithmic ratio between the spiral pS-FRs from different tracers peaks around 0, and the small offsets in some plots are consistent with the errors in the conversion factors in K09. E and S0 galaxies from our sample are plotted in shaded histograms. These plots show that the TIR consistently overestimates the SFR in E/S0s when compared to the two mid-IR tracers. The 8 and $24\mu m$ tracers are in very good agreement. The plots with radio as a tracer show the widest spread in both the spirals and E/S0s. The bin with an arrow in the $24\mu m$ versus radio histogram represents NGC 2768 which has a logarithmic ratio of -1.4.

Figure 13. Unobscured pSFR (traced by Hα) compared to the obscured pSFRs (traced by $8\mu m$ PAHs in red, $24\mu m$ in blue and TIR in green). Our sample E/S0s are plotted as large filled stars, with the LVL sample plotted as unfilled symbols for comparison. A one-to-one line is plotted indicating equal contributions from unobscured and obscured SF.

their large scatter. Taking an example from our sample, the known radio AGN NGC 2768 does not lie off the Schmidt-Kennicutt law when its SFR is determined with radio+Hα (although it is a bit above the constant SFE range). Similarly, the overestimation of SFR by the TIR does not move galaxies completely off either relation. If we assume that the 24 and $8\mu m$ PAH emission are the most accurate tracers of the obscured SFR, then galaxies still occupy a large range.

A lower star formation efficiency is expected for early-type galaxies based on the morphological quenching model of Martig et al. (2009), due to the lack of a stellar disc to aid the development of gas instabilities. If the Schmidt-Kennicutt law is the correct description of how stars form from gas, then we only see some tentative signs that early-type galaxies may be less efficient at converting gas into stars when using the Hα + $24\mu m$ tracer. No bias towards inefficiency is found with respect to the constant SFE relation of Bigiel et al. (2008).

7 CONCLUSIONS

We present new molecular gas maps for the three early-type galaxies NGC 524, NGC 3489 and NGC 4477. The molecular gas distribution of NGC 3489 shows spiral structure within an S0 galaxy for the first time. Strong upper limits on the molecular gas content of NGC 4278 and NGC 7457 are also reported (previously considered detections in the literature). With these new maps, we now have a sample of 13 E/S0 galaxies with optical IFU coverage and CO detections, 12 of which also have CO maps.

The distribution of molecular gas in our sample galaxies is generally central, in settled rings or discs, although there are also a few cases of more externally distributed molecular gas. Optically-obscuring dust is always found co-

This good agreement is surprising - the galaxies without observed young stars or dominant ongoing star formation lie on the relations just as galaxies with significant AGN. However, neither law has particularly stringent bounds. For example, a galaxy with an average gas density of 70 M$_\odot$ pc^{-2} (typical for our sample) could have a SFR surface density anywhere between 0.024 and 0.153 M$_\odot$ kpc^{-2} by the Schmidt-Kennicutt law, a range of nearly an order of magnitude. AGN, old stars and other sources of ionisation and dust heating do not contribute enough to move the galaxies outside of the wide range allowed by the relations. In fact, these same sources may be present in the galaxies used to define the star-formation laws in the first place, explaining

incident with the molecular gas distributions, and reveals tightly-wound spiral discs in the galaxies that contain more than around 10^8 M$_\odot$ of molecular gas. Average molecular gas surface densities range between 10 and 250 M$_\odot$ pc^{-2} across the sample.

Comparing IFU and CO maps, we find that the ionised gas and molecular gas are connected in early-type galaxies. Ionised gas is present wherever we detect molecular gas and the two phases always have aligned rotation. In about half the galaxies, the ionised gas is even more extended than the molecular gas. These are the same galaxies that have high [O III]/Hβ ratios, indicating that a process other than star formation dominates their gas ionisation. Young stellar populations are detected through a mix of optical colours, UV-optical colours and absorption linestrength maps. Young or intermediate populations are more extended than the molecular gas in 6/11 galaxies, coincident with the molecular gas in 2/11 galaxies and not present in 3/11 galaxies.

Combining information on the gas ionisation and stellar populations of our sample of galaxies, a loose classification is suggested. First are obviously star-forming galaxies. These galaxies have low [O III]/Hβ emission line ratios and clearly-detected young stellar populations. They also host larger quantities of molecular gas ($> 10^8$ M$_\odot$). Second are post-starburst galaxies with high [O III]/Hβ ratios, but still widespread young stellar populations. They likely had more widespread and higher rates of star formation in the recent past, and are now exhausting their relatively small molecular gas reservoirs ($< 10^8$ M$_\odot$). The final category contains galaxies where any star formation from the molecular gas is not significant enough to lower the [O III]/Hβ ratio or produce a detectable young stellar population. These galaxies have similar properties to E/S0s without any molecular gas. The 13 early-types we study here are almost equally distributed between these three categories.

E/S0s with molecular gas do not follow the radio-FIR correlation. A few of our sample galaxies host radio AGN and have excess radio continuum flux compared to FIR flux, but most E/S0s fall on the FIR-excess side of the relation. The 8 and 24μm star formation tracers agree well for E/S0 galaxies, but the TIR overestimates the SFR by an average factor of around 2.8, presumably because of additional heating by older low-mass stars. The pSFRs based on our calculated Hα values are very similar to the values of the IR pSFRs, indicating that our galaxies do not vary widely in their degree of obscuration and have gas-phase metallicities more similar to those of spirals than metal-poor dwarfs.

We find that our E/S0 galaxies mostly lie within the large ranges of the Schmidt-Kennicutt law of Kennicutt (1998b) and the constant star-formation efficiency law as described in Bigiel et al. (2008). This agreement suggests that star formation in early-type galaxies with molecular gas is not extremely different from that observed in spiral or starburst galaxies.

REFERENCES

Bacon R. et al., 2001, MNRAS, 326, 23
Baum C. W., 1959, PASP, 71, 106
Bigiel F., Leroy A., Walter F., Brinks E., de Blok W. J. G., Madore B., Thornley M. D., 2008, AJ, 136, 2846
Bohlin R. C., Savage B. D., Drake J. F., ApJ, 224, 132
Bower R. G., Lucey, J. R., Ellis R. S., 1992, MNRAS, 254, 601
Calzetti D. et al., 2005, ApJ, 633, 871
Calzetti D. et al., 2007, ApJ, 666, 870
Cappellari M., Copin Y., 2003, MNRAS, 342, 345
Cappellari M., Emsellem E., 2004, PASP, 116, 138
Cappellari M. et al., 2006, MNRAS, 366, 1126
Cappellari M. et al., 2007, MNRAS, 379, 418
Cardelli J. A., Clayton G. C., Mathis J. S., ApJ, 345, 245
Colbert E. J. M., Mushotzky R. F., 1999, ApJ, 519, 89
Combes F., Young L.M., Bureau M., 2007, MNRAS, 377, 1795
Condon J. J., Anderson M. L., Helou G., 1991, ApJ, 376, 95
Condon J. J., Cotton W. D., Greisen E. W., Yin Q. F., Perley R. A., Taylor G. B., Broderick J. J., 1998, AJ, 115, 1693
Condon J. J., Cotton W. D., Broderick J. J., 2002, AJ, 124, 675
Crocker A. F., Bureau M., Young L. M., Combes F., 2008, MNRAS, 386, 1811
Crocker A. F., Jeong H., Komugi S., Combes F., Bureau M., Young L. M., Yi S., 2009, MNRAS, 393, 1255
Dale D. A., Helou G., 2002, ApJ, 576, 159
Dale D. A. et al., 2009, ApJ, 703, 517
de Vaucouleurs G., de Vaucouleurs A., Corwin H. G., Buta R. J., Paturel G., Fouque P., 1991, Third Reference Cat-

alog of Bright Galaxies, Vols. 1-3, XII. Springer-Verlag, Berlin (RC3)

de Zeeuw T., et al., 2002, MNRAS, 329, 513

di Serego Alighieri S., 2007, A&A, 474, 851

Djorgovski S., Davis M., 1987, ApJ, 313 59

Doi A., Kameno S., Kohno K., Nakanishi K., Inoue M., 2005, MNRAS, 363, 692

Donovan J. et al., 2009, ApJ, 137, 5037

Donzelli C. J., Davoust E., 2003, A&A, 409, 91

Dressler A., Lynden-Bell D., Burstein D., Davies R. L., Faber S. M., Terlevich R., Wegner G., 1987, ApJ, 313, 42

Emsellem E., et al., 2004, MNRAS, 352, 721

Emsellem E., et al., 2007, MNRAS, 379, 401

Faber S. M., Gallagher J. S., 1976, ApJ, 204, 365

Faber S. M., Dressler A., Daview R. L., Burstein D., Lynden-Bell D., 1987, in Nearly Normal Galaxies: From the Planck Time to the Present, ed. S. M., Faber (New York: Springer), 175

Filho M. E., Barthel P. D., Ho L. C., 2002, ApJS, 142, 223

Filho M., Fraternali F., Markoff S., Nagar N., Barthel P., Ho L., Yuan F., 2004, A&A, 418, 429

Giovannini G., Cotton W. D., Feretti L., Lara L., Venturi T., 2001, ApJ, 552, 508

Guilloteau S., Lucas R., 2000, in Mangum J.G., Radford S.J.E., eds, ASP Conf. Ser. Vol. 217, Imaging at Radio through Submillimeter Wavelengths. Astron. Soc. Pac., San Francisco, p. 299

Högbom J.A., 1974, A&AS, 15, 417

Jansen R. A., Fabricant D., Franx M., Caldwell N., 2000, ApJS, 126, 331

Jeong H., Bureau M., Yi S. K., Kranjovi D., Davies R., 2007, MNRAS, 376, 1021

Jeong H. et al. 2009, MNRAS, 398, 2028

Johnson D. W., Gottesman S. T., 1979, in Photometry, Kinematics, and Dynamics, ed. D. S. Evans (Austin: University of Texas Press), p. 57

Jura M., 1982, ApJ, 254, 70

Kawata D., Cen R., Ho L. C., 2007, ApJ, 669, 232

Kennicutt R. C., 1998a, ARA&A, 36, 189

Kennicutt R. C., 1998b, ApJ, 498, 541

Kennicutt R. C., Lee, J. C., Funes S., J., José G., Sakai, S., Akiyama S., 2008, ApJS, 178, 247

Kennicutt R. C. et al., 2009, ApJ, 703, 1672

Kewley L. J., Geller M. J., Jansen R. A., Dopita M. A., 2002, AJ, 124, 3135

Knapp G. R., Guhathakurta P., Kim D., Jura M.A., 1989, ApJS, 70, 329

Knapp G. R., Rupen M. P., 1996, ApJ, 460, 271

Kormendy J., Fisher D. B. Cornell M. E., Bender R., 2009, ApJS, 182, 216

Krips M. et al., 2007, A&A, 464, 553

Kuntschner H., et al., 2006, MNRAS, 369, 497

Kuntschner H., et al., 2010, MNRAS, accepted

Lee J. C. et al., 2009, ApJ, 706, 599

Lonsdale Persson C. J., Helou G., 1987, ApJ, 314, 513

Lucero D. M., Young L. M., 2007, AJ, 134, 2148

Lucero D. M., Young L. M., 2008, AIPC, 1035, 135

Martig M., Bournaud F., Teyssier R., Dekel A., 2009, ApJ, 707, 250

McDermid R.M., et al., 2006, MNRAS, 373, 906

Morganti R. et al., 2006, MNRAS, 371, 157

Nilson P., 1973, Uppsala General Catalogue of Galaxies.

Nova Acta Regiae Soc. Sci. Upsaliensis Astronomiska Observatorium, Uppsala

O'Connell R. W., 1999, AR&A, 37, 603

Okuda T., Kohno K., Iguchi S., Nakanishi K., 2005, ApJ, 620, 673

Osterbrock D. E., 1989, Astrophysics of Gaseous Nebulae and Active Galactic Nuclei (Mill Valley: University Science Books)

Price R., Duric N., 1992, ApJ, 401, 81

Roussel H., Sauvage M., Vigroux L., Bosma A., 2001, A&A, 372

Sánchez-Blázquez P. et al., 2006, MNRAS, 371, 703

Sarzi M. et al. 2006, MNRAS, 366, 1151

Sarzi M. et al. 2010, MNRAS, 402, 2187

Schawinski K., Thomas D., Sarzi M., Maraston C., Kaviraj S., Joo S.-J., Yi S. K., Silk J., 2007, MNRAS, 382, 1415

Schawinski K. et al., 2007, ApJS, 173, 512

Schilizzi R. T., Fanti C., Fanti R., Parma P., 1983, A&A, 126, 412

Schinnerer E., Scoville N., 2002, ApJ, 577, L103

Schmidt M., 1959, ApJ, 129, 243

Scott N. et al., 2009, MNRAS, 398, 1835

Shapiro K., et al., 2010, MNRAS, 402, 2140

Sil'chenko O. K., 2000, AJ, 120, 741

Taniguchi Y., Murayama T., Nakai N., Suzuki M., Kameya O., 1994, ApJ, 108, 468

Temi P., Brighenti F., Matthews W.G., 2007, ApJ, 660, 1215

Temi P., Brighenti F., Matthews W.G., 2009a, ApJ, 695, 1

Temi P., Brighenti F., Matthews W.G., 2009b, ApJ, 707, 890

Thomas D., Maraston C., Bender R., Mendes de Oliveira C., 2005, ApJ, 621, 673

Trager S. C., Faber S. M., Worthey G., González J. J., 2000, AJ, 120, 165

Visvanathan N., Sandage A., 1977, ApJ, 216, 214

Walsh D. E. P., Knapp G. R., Wrobel J. M., Kim D.-W., 1989, ApJ, 337, 209

Welch G. A., Sage L. J., 2003, ApJ, 584, 260

Weijmans A.-M., Kranjovi D., van de Ven G., Oosterloo T., Morganti R., de Zeeuw P. T., 2008, MNRAS, 383, 1343

Wiklind T., Henkel C., 1989, A&A, 225, 1

Wiklind T., Henkel C., 1995, A&A, 297, L71

Wiklind T., Combes F., Henkel C., Wyrowski, F., 1997, A&A, 323, 727

Wu H., Cao C., Hao C.-N., Liu F.-S., Wang J.-L., Xia X.-Y., Deng Z.-G., Young C. K.-S., 2005, ApJ, 632, L79

Yi, S. K., et al., 2005, ApJ, 610, L111

Young J. S., Scoville N. Z., 1991, ARA&A, 29, 581

Young J. S., Allen L., Kenney J. D. P., Lesser A., Rownd, B., 1996, AJ, 112, 1903

Young L. M., 2002, ApJ, 124, 788

Young L. M., 2005, ApJ, 634, 258

Young L. M., Bureau M., Cappellari M., 2008, ApJ, 676, 317

Young L. M., Bendo G. J., Lucero D. M., 2009, AJ, 137, 3053

Yun M. S., Reddy N. A., Condon J. J., 2001, ApJ, 554, 803

APPENDIX A: SAURON MAPS OF NGC 2320 AND NGC 5666

Being outside of the main SAURON sample, the IFU maps of NGC 2320 and NGC 5666 have not previously been published. We present these maps in Figs. A1 and A2, then briefly summarise the properties revealed for each galaxy.

Observations of NGC 2320 and NGC 5666 were taken during SAURON run 1 and run 8, with 4×1800s and 3×1800s exposures, respectively. Bacon et al. (2001) describes the steps taken in the XSAURON software to create the datacube: bias and dark subtraction, extraction of the spectra, wavelength calibration, flat-fielding, cosmic ray removal, sky subtraction and flux calibration. The stellar kinematics are fit using the penalised pixel fitting method (pPXF, Cappellari & Emsellem 2004) and the gas emission and kinematics are fit using GANDALF (Gas AND Absorption Line Fitting algorithm; Sarzi et al. 2006). The linestrengths are determined as described in Kuntschner et al. (2006). Due to the higher recessional velocity of NGC 2320, the Mgb line was redshifted out of the SAURON wavelength range and is thus not available. The maps are made using data Voronoi binned spatially (Cappellari & Copin 2003) to a minimum signal to noise of ≈ 60 per spectral pixel.

A1   NGC 2320

The stellar velocity map of NGC 2320 shows clear rotation and its stellar velocity dispersion map has a central peak (see Fig. A1). The third and fourth Gauss-Hermite moments are noisy. Based on these data, Cappellari et al. (2007) calculate a λ_{R_e} parameter for NGC 2320 of 0.34, a measure of the projected stellar angular momentum per unit mass. NGC 2320's relatively high value puts it into the class of fast-rotating galaxies, which is surprising given its large mass. On a diagram of λ_{R_e} versus virial mass, NGC 2320 clearly sticks out; all other such massive galaxies are slow rotators (see fig. 11 of Emsellem et al. 2007).

The ionised gas in NGC 2320 corotates with the stars. The high central gas velocity dispersion points to AGN activity, which is supported by the peaks in the equivalent widths of both the [O III] and Hβ emission lines and the compact radio emission observed by Lucero & Young (2007). The [OIII] equivalent width map shows a structure elongated along the major axis of the galaxy. The [O III]/Hβ ratio is high throughout the region of detected emission, indicating that star formation is unlikely to be dominating the ionisation. The luminosity-weighted average Hβ and Fe5015 absorption linestrengths within $R_e/8$ (4.6 arcsec) are 1.80 and 5.11 Å, respectively. Outside of this radius, the bins become much bigger and the signal-to-noise is marginal for measuring linestrengths, as is evidenced by the wide spread in adjacent bins. Unfortunately, the Mgb feature is redshifted outside of the SAURON spectral range for this galaxy.

A2   NGC 5666

NGC 5666 has an obvious face-on star-forming ring in its centre (see Fig. A2). The stellar kinematics show that the rotation of the ring is aligned with the rest of the galaxy and there are signs of a slightly lower stellar velocity dispersion within the ring.

The ring can be seen clearly in the flux and equivalent width maps for both the Hβ and [O III] emission lines. Moreover, hot spots can be seen within the ring, presumably the sites of the most active star formation. The entire region has a low [O III]/Hβ ratio that can only be caused by star formation. The gas rotates like the stars and has no central dispersion peak to suggest an AGN.

The linestrengths also fit the picture of a star-forming ring. The Hβ linestrength is high everywhere, but highest in the ring. Breaking the galaxy into three projected regions of radius under 3 arcsec, radius between 3 and 9 arcsec and radius over 9 arcsec, the luminosity-averaged Hβ linestrengths are 3.17, 3.56 and 3.33 Å. Young stars must contribute to this high linestrength everywhere, but even more so within the ring. Low Mgb and Fe5015 values are found in the ring and outside of it but both clearly peak in the centre. Mgb is partially age-sensitive and decreases with a young stellar population, as is clearly seen in the youngest SAURON galaxies (NGC 3032, NGC 3156, NGC 4150). The Fe5015 index is less age sensitive and the low values in NGC 5666 may suggest a genuine low-metallicity population (as in NGC 3032; Kuntschner et al. 2010).
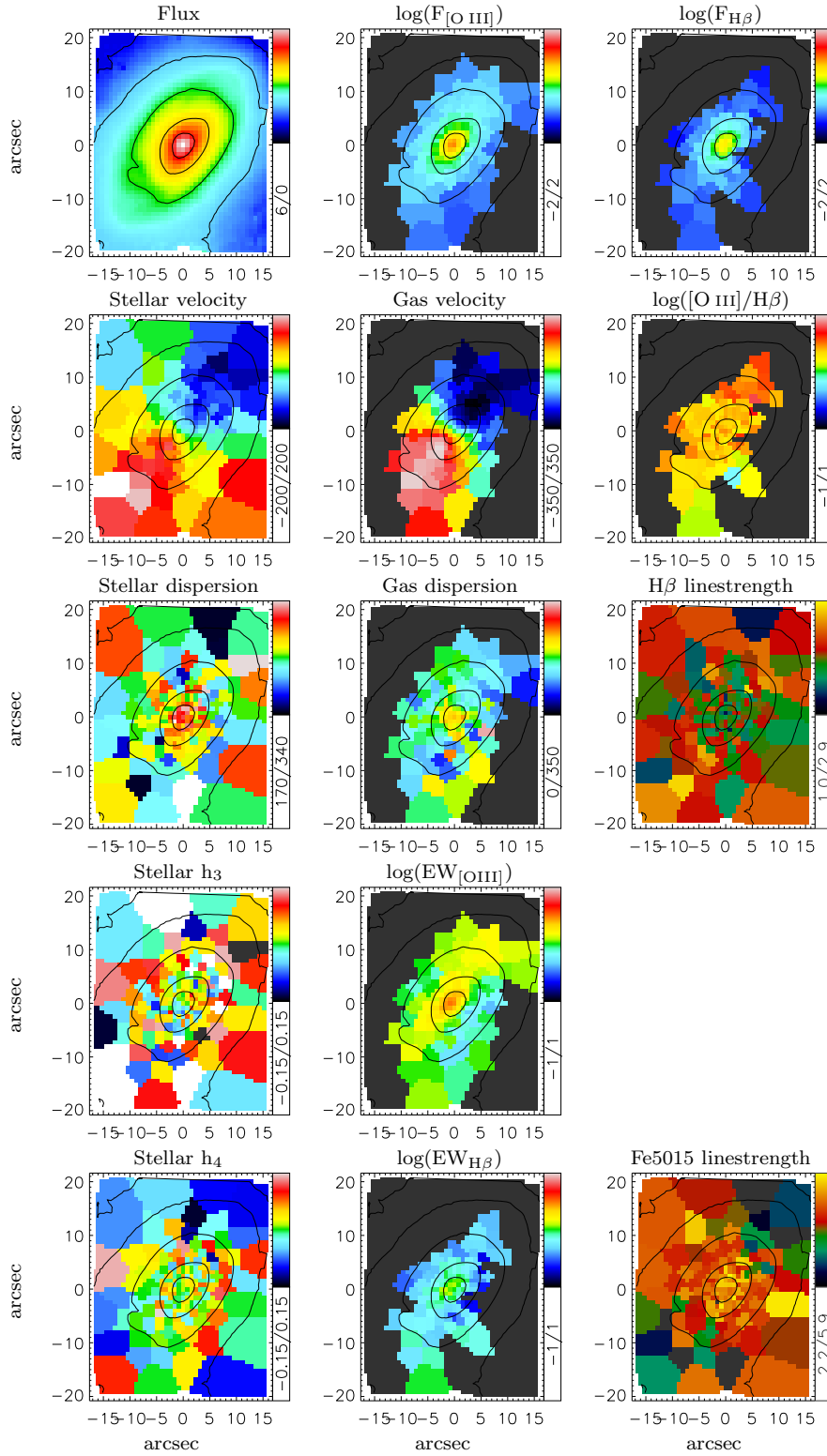
Figure A1. SAURON maps of NGC 2320. From top to bottom, left to right: *first column* – reconstructed intensity (arbitrary units), mean stellar velocity (km s^{-1}), stellar velocity dispersion (km s^{-1}), stellar Gauss-Hermite coefficients h_3 and h_4 (dimensionless); *second column* – [O III] emission line flux (10^{-16} erg s^{-1} cm^{-2} arcsec^{-2}), [O III] velocity (km s^{-1}), [O III] velocity dispersion (km s^{-1}), [O III] equivalent width (Å), Hβ equivalent width (Å); *third column* – Hβ emission line flux (10^{-16} erg s^{-1} cm^{-2} arcsec^{-2}), [O III]/Hβ line ratio (dimensionless), Hβ Lick absorption line index (Å), Fe5015 Lick absorption line index (Å). The isophotes over-plotted are in half-magnitude steps. Grey bins in the emission-line maps indicate that emission was not detected.
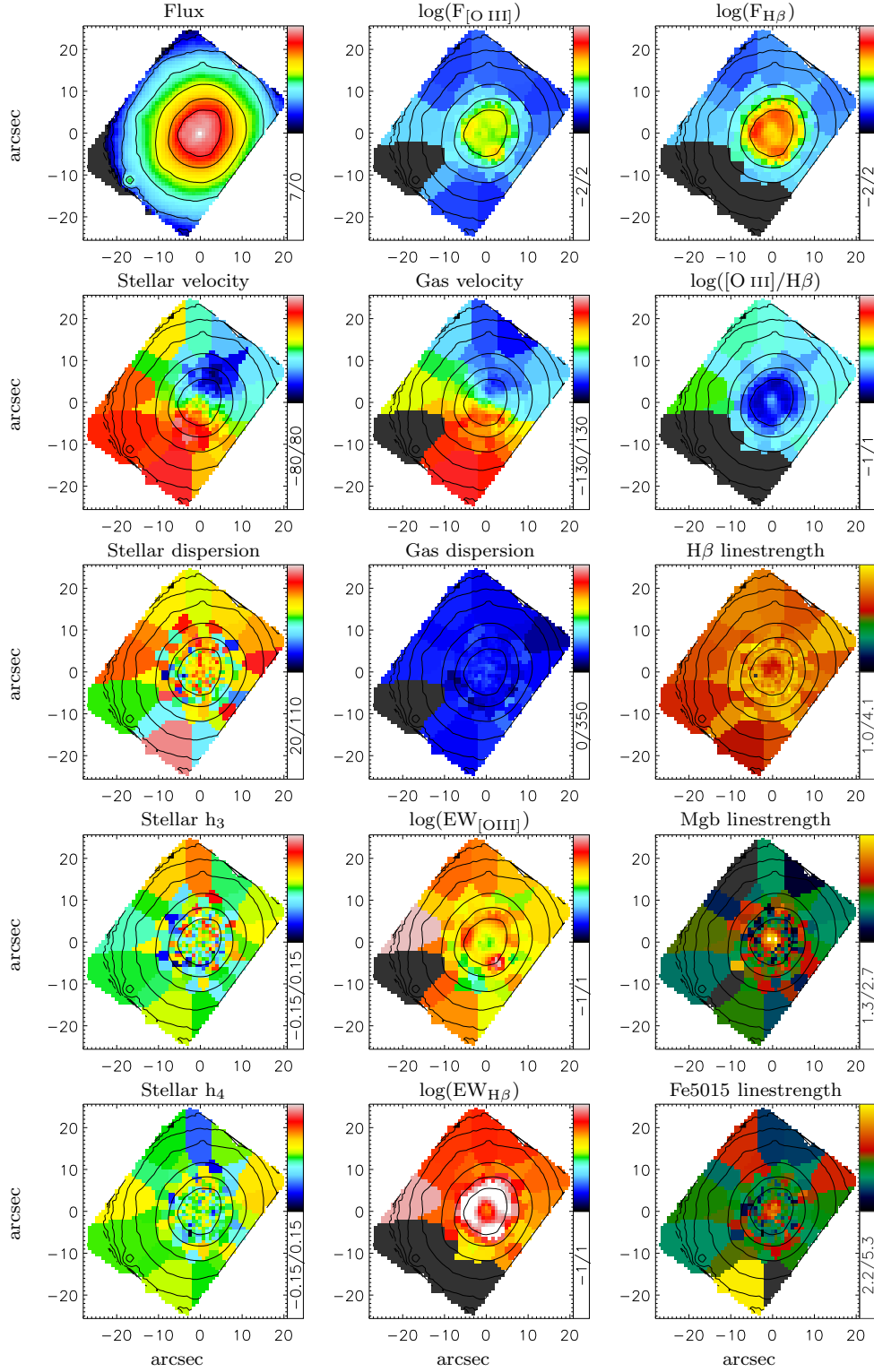
Figure A2. SAURON maps of NGC 5666. From top to bottom, left to right: *first column* – reconstructed intensity (arbitrary units), mean stellar velocity (km s^{-1}), stellar velocity dispersion (km s^{-1}), stellar Gauss-Hermite coefficients h_3 and h_4 (dimensionless); *second column* – [O III] emission line flux (10^{-16} erg s^{-1} cm^{-2} arcsec^{-2}), [O III] velocity (km s^{-1}), [O III] velocity dispersion (km s^{-1}), [O III] equivalent width (Å), Hβ equivalent width (Å); *third column* – Hβ emission line flux (10^{-16} erg s^{-1} cm^{-2} arcsec^{-2}), [O III]/Hβ line ratio (dimensionless), Hβ Lick absorption line index (Å), Mgb Lick absorption line index (Å), Fe5015 Lick absorption line index (Å). The isophotes over-plotted are in half-magnitude steps. Grey bins in the emission-line maps indicate that emission was not detected.